University of Alberta

AXISYMMETRIC INTERNAL SOLITARY WAVES LAUNCHED BY
RIVER PLUMES

by

Justine M. McMillan

A thesis submitted to the Faculty of Graduate Studies and Research in partial fulfillment of the
requirements for the degree of

Master of Science

Department of Physics

©Justine M. McMillan
Spring 2011
Edmonton, Alberta

Examining Committee

Bruce Sutherland, Physics & Earth and Atmospheric Sciences

Martyn Unsworth, Physics & Earth and Atmospheric Sciences

Morris Flynn, Mechanical Engineering

Gordon Swaters, Mathematical and Statistical Sciences

Abstract

The generation and evolution of internal solitary waves by intrusive gravity currents and river plumes are examined in an axisymmetric geometry by way of theory, experiments and numerical simulations. Full depth lock-release experiments and simulations demonstrate that vertically symmetric intrusions propagating into a two-layer fluid with an interface of finite thickness can launch a mode-2 double humped solitary wave. The wave then surrounds the intrusion head and carries it outwards at a constant speed. The properties of the wave's speed and shape are shown to agree well with a Korteweg-de Vries theory that is derived heuristically on the basis of energy conservation. The numerical code is also adapted to oceanographic scales in an attempt to simulate the interaction between the ocean and a river plume emanating from the mouth of the Columbia River. Despite several approximations, the fundamental dynamics of the wave generation process are captured by the model.

Acknowledgements

Table of Contents

List of Tables

List of Figures

Chapter 1

Introduction

1.1 Motivation

Internal waves, which propagate along density interfaces within a stratified fluid, are commonly observed in the coastal ocean (Jackson, 2004). These waves can attain large amplitudes with respect to the local fluid depth, and if they propagate with a constant speed and unvarying shape, they are referred to as "internal solitary waves". Because solitary waves can transport both mass and momentum they are responsible for the redistribution and mixing of nutrients in coastal regions.

Internal solitary waves are visualized from space using synthetic aperture radar (SAR) which measures backscatter signals from the ocean surface. SAR images of internal waves consist of periodic dark and bright bands, which correspond to surface regions of enhanced smoothness and roughness, respectively. The smooth regions arise ahead of the wave peaks where the horizontal velocities are diverging, whereas the rough regions arise ahead of the wave troughs, where the horizontal velocities are converging. Over 300 observations, from 54 regions of the world, are presented in the *Atlas of Oceanic Internal Solitary Waves* (Jackson, 2004). Although the images have a spatial resolution as fine as a couple metres (Pan et al., 2007), it is difficult to measure the characteristics of the waves' vertical structure from the top-view perspective.

The advancement of ocean instrumentation, and specifically the development of thermistor arrays, in the 1960s and 1970s motivated several observational *in situ* studies of internal solitary waves (Helfrich and Melville, 2006). For example, waves were measured in the Andaman Sea (Perry and Schimke, 1965), the Strait of Gibraltar (Ziegenbein, 1969) and the Massachusetts Bay (Halpern, 1971), among other locations. These, and related studies, demonstrated that internal solitary waves can be generated by tidal currents flowing over bottom topography, including shelf breaks and sills.

In the absence of topography, internal solitary waves can be launched by gravity currents, which arise when a fluid of one density flows horizontally into an ambient fluid of a different, or varying, density. In the ocean, these currents may be manifest in the form of river plumes (Nash and Moum, 2005). At high tide the ocean water forces the river water upstream. Then, as the tide relaxes, ebb currents begin to flow allowing the fresh water from the river to propagate along the surface of the coastal ocean. These plumes force the denser near-surface ocean waters downwards launching an internal wave which is manifest as an undulation of the pycnocline.

A distinguishing feature of SAR images of internal waves is that the fronts tend to have some degree of curvature, regardless of whether the waves are launched by localized topography or gravity currents. Most of the previous experimental and theoretical attempts to characterize the dynamics of internal solitary waves have been limited to a rectilinear geometry which does not describe the lateral spreading of the waves as they propagate away from their source. The major thrust of this thesis is to extend earlier research into rectilinear internal waves to the study of radially spreading internal waves.

1.2 Background

In this work, we focus on the generation of internal solitary waves from gravity currents and "intrusions", which are gravity currents that propagate at an intermediate level between the upper and lower boundaries of a fluid along their level of neutral buoyancy. We begin by reviewing existing experimental and theoretical research on gravity currents and internal solitary waves in both rectilinear and axisymmetric geometries.

1.2.1 Rectilinear Gravity Currents and Intrusions

Gravity currents are often studied in the laboratory by way of lock-release experiments where two fluids of different densities are initially separated by a vertical lock (e.g. see Simpson (1997)). The lock is then rapidly extracted causing the denser fluid to flow beneath the lighter fluid. The propagation of gravity currents can be divided into three distinct phases: the slumping phase, the inertial (or self-similar) phase and the viscous phase. The slumping phase occurs immediately after the lock removal and it is characterized by a gravity current that moves at a constant velocity. In the inertial phase, the current thins and decelerates, as the motion is dominated by buoyancy and inertial forces. The viscous phase occurs when the motion is so slow and the current is so thin that its evolution is dominated by the viscous and buoyancy forces (Huppert, 1982).

Lock-release experiments of "symmetric" intrusions have been performed in an approximate two-layer fluid with equal upper- and lower-layer depths in which the intrusion density was the average ambient density (Britter and Simpson, 1981; Faust and Plate, 1984; Rooij et al., 1999; Lowe et al., 2002). By symmetry, such studies are equivalent to the examination of surface gravity currents moving across a free-slip boundary in a stratified ambient. Unlike

gravity currents in uniform ambients, which are predicted to transition to the inertial phase and decelerate after propagating 6 to 10 lock lengths (Rottman and Simpson, 1983), symmetric intrusions at sufficiently thick interfaces were found to propagate well beyond this distance at a constant speed (Mehta et al., 2002; Sutherland and Nault, 2007). In a rectilinear geometry, intrusions maintained a constant speed beyond 22 lock lengths. For small, but finite interface thicknesses, the measured speed was faster than the linear long wave speed, suggesting that the intrusion generated a solitary wave. Subsequently, the closed-core solitary wave carried the intrusion outwards. The waves were observed in intrusion experiments because the stratification at the interface supported the formation of a wave. Similarly, if a surface gravity current propagated into a thin stratified layer (the symmetric extension of a symmetric intrusion at a thin interface), its speed was constant well beyond 10 lock lengths (Sutherland and Nault, 2007).

1.2.2 Axisymmetric Gravity Currents

The dynamics of radially spreading gravity currents are qualitatively different from rectilinear gravity currents because energy and mass conservation require the head height to decrease. Hence the current should decelerate soon after release due to the reduction of the horizontal pressure gradient driving the flow. Lock-release experiments (Huppert and Simpson, 1980; Didden and Maxworthy, 1982; Huq, 1996; Hallworth et al., 1996; Patterson et al., 2006) demonstrated that axisymmetric bottom-propagating gravity currents maintain a constant speed up to 3 lock radii. Thereafter, in the inertial phase, the position of the front changed as $t^{1/2}$, consistent with the theory (Hoult, 1972; Huppert and Simpson, 1980) that assumes the current maintains a self-similar cylindrical shape. By symmetry, Zemach and Ungarish (2007) used shallow water theory to extend this prediction to axisymmetric intrusion propagation,

again predicting that the intrusion decelerates shortly after release from the lock.

Contrary to this prediction, full-depth lock release experiments demonstrated that axisymmetric intrusions propagate at a constant speed well beyond 3 lock radii (Sutherland and Nault, 2007). This suggested that, as in a rectilinear geometry, solitary waves were responsible for transporting the lock-fluid long distances at a constant speed. The experiments thus put into question the applicability of shallow water theory, which necessarily filters the albeit weakly non-hydrostatic dynamics of solitary waves. However, the experimental analysis did not go on to study the wave generation and evolution process.

Axisymmetric intrusions are symmetric expansions of the experiments by Maxworthy (1980), who launched a solitary wave by releasing a bottom-propagating gravity current into an ambient consisting of a shallow stratified layer beneath a uniform density fluid. He observed that the front velocity of the wave was nearly constant until its amplitude decreased beyond a critical value. After this time the front position changed according to $r \sim t^{2/3}$.

In part of the work presented here, we will examine the advance of intrusions in different ambient densities. This will be done through the analysis of experiments and numerical simulations.

1.2.3   Axisymmetric Solitary Waves

As explained in Section 1.1, the motivation for this work arises in part from the observation of laterally spreading internal solitary waves, for which theory is limited. In a rectilinear geometry, the weakly nonlinear Korteweg-de Vries (KdV) model is appropriate if nonlinearity and nonhydrostatic dispersion are comparable and small. Large amplitude closed-core solitary waves can be accurately described by the fully nonlinear Dubreil-Jacotin-Long (DJL) equation

(Dubreil-Jacotin, 1937; Long, 1953, 1956).

Following up upon the work of Miles (1978), Weidman and Velarde (1992) developed a theory for axisymmetric internal solitary waves within a stratified ambient fluid. They predicted an amplitude dependence upon distance as $r^{-2/3}$. But, in an earlier paper, Weidman and Zakhem (1988) compared this amplitude prediction with experiments by Maxworthy (1980) and found that the amplitude differed by up to 34%. They explained that their weakly nonlinear theory did not capture the experimental results because the trapping of the mixed fluid was "a clear manifestation of strong nonlinear effects". They admitted, however, that their equation was asymptotically inconsistent and so its predictions were not necessarily reliable. The theory presented by Weidman and Velarde (1992) likewise relied upon inconsistent assumptions.

Part of the work presented here uses numerical simulations to examine radially spreading solitary waves. From these observations, a heuristic theory is developed to describe their evolution. Ultimately the goal of this thesis is to provide some insight into the observed dynamics of solitary waves generated by river plumes.

1.3   Thesis Overview

In this work we use theory, experiments and numerical simulations to characterize the dynamics of internal solitary waves in an axisymmetric geometry[1]. The thesis is organized such that the theory is summarized in Chapter 2, the experiments are summarized in Chapter 3, and the numerical simulations are summarized in Chapters 4–6.

More specifically, Chapter 2 outlines the theory governing the speed of a vertically symmetric intrusion as a function of interface thickness. The theories

---

[1]Sections of Chapters 2 and 5 have been published: Justine M. McMillan and Bruce R. Sutherland (2010). *Nonlinear Processes in Geophysics*. 17: 443–453.

of axisymmetric linear waves and rectilinear solitary waves are then reviewed before discussing two theories for cylindrical solitary waves. One theory was derived rigorously using perturbation methods whereas the other was obtained heuristically on the basis of an energy conservation assumption.

Chapter 3 discusses experiments of intrusions that were conducted in a cylindrical tank. In the idealized setup, the intrusion was released from a full-depth lock into an approximately two-layer ambient with equal upper- and lower-layer depths. For all experiments, the density of the intrusion was equivalent to the average density of the ambient fluid. The analysis methods and results of measuring intrusion speeds are also provided in Chapter 3.

Chapter 4 describes the fully nonlinear numerical code that was used for the simulation of axisymmetric internal waves. A discussion of how the code was used to simulate intrusions is provided in Chapter 5, in which the results are also compared to the idealized experiments of Chapter 3.

Chapter 6 explains how the code was used to simulate a river plume emanating from the Columbia River and its consequent interaction with the thermocline. The results of these simulations are then compared to the observations of Nash and Moum (2005).

Finally, in Chapter 7 a summary of the significant results of this work is presented and directions for future work are suggested.

Chapter 2

Theory

This work involves the study of radially spreading intrusions and the interfacial waves they generate. We begin by adapting existing theory for rectilinear gravity currents in a uniform density fluid and in a uniformly stratified fluid to develop a prediction for the speed of intrusions at interfaces of arbitrary thickness. This analysis is restricted to the study of symmetric intrusions, meaning that the density of the intrusion is the average ambient density and the background density gradient is itself symmetric in the vertical. In Chapters 3 and 5, we proceed to compare the speeds of experimental and simulated radial intrusions with the rectilinear theory prediction. In doing so, we evaluate the effect of the initial curvature of the intrusion front upon setting the radial intrusion speed.

Being symmetric, the intrusion most efficiently excites a mode-2 interfacial wave, which bulges upwards above and downwards below the mid-depth of the interface. These waves are sometimes referred to as being "varicose" because of the double-humped shape of the isopyncals. A schematic comparing mode-1 and mode-2 waves is shown in FIgure 2.1. We briefly review the theory for small-amplitude long interfacial waves with this mode-2 structure. Finally, we review Korteweg-de Vries (KdV) theory for rectilinear solitary waves in continuously stratified fluid. We then describe an adaptation of this theory
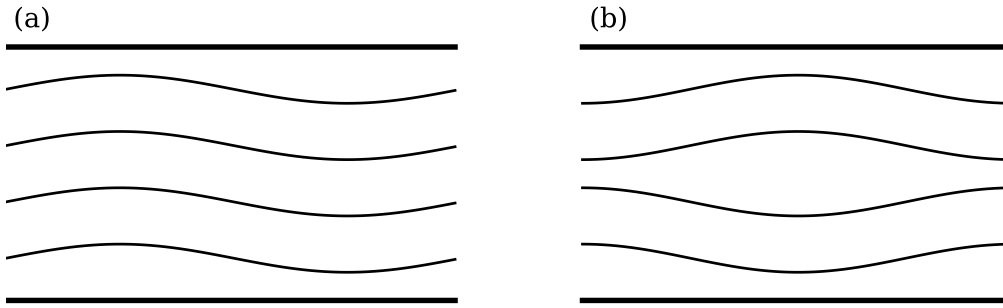
Figure 2.1: Schematic showing the deflection of isopycnals for (a) mode-1 and (b) mode-2 waves in a vertically bounded domain.

for radially spreading solitary waves that is later compared to observations.

2.1 Rectilinear speed of a symmetric intrusion at a thick interface

The speed of a rectilinear intrusion at an interface of finite thickness was first predicted by Ungarish (2005) using a shallow water model. That said, his result underpredicted the experimental speeds measured by Faust and Plate (1984). These experiments were well described, however, by White and Helfrich (2008) who used a fully nonlinear Dubreil-Jacotin-Long (DJL) approach to describe an intrusion at a finite-thickness interface. But that theory too is limited because recent experiments and simulations by Bolster et al. (2008) suggest that the theory of White and Helfrich (2008) overpredicts the intrusion speed for the limit of a linearly stratified ambient. In this limit, DJL theory is obviously flawed because it unphysically requires the head height of the intrusion to tend to zero.

Rather than adapt DJL theory, here we take the simplest approach to predict the rectilinear intrusion speed while ensuring that our result is in agreement with the predictions for two-layer and linearly stratified ambients. The
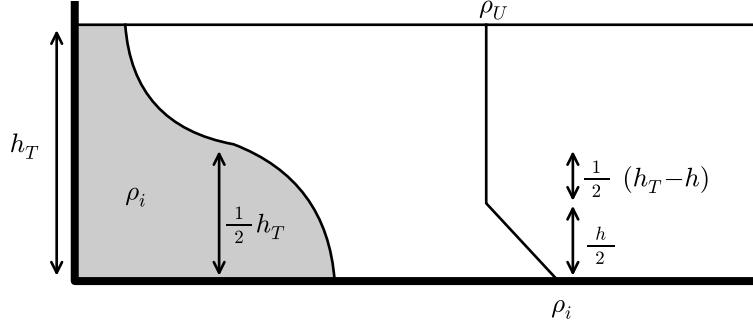
Figure 2.2: The domain and the density profile used to derive a theory for the speed of intrusions as a function of interface thickness.

background density profile, $\bar{\rho}$, is assumed to have the piecewise-linear form,

$$\bar{\rho}(z) = \begin{cases} \rho_{\mathrm{U}} & \frac{h}{2} < z < \frac{H}{2} \\ \rho_i + \frac{z}{h}\left(\rho_{\mathrm{U}} - \rho_{\mathrm{L}}\right) & -\frac{h}{2} \leq z \leq \frac{h}{2} \\ \rho_{\mathrm{L}} & -\frac{H}{2} < z < -\frac{h}{2}, \end{cases} \tag{2.1}$$

where h is the thickness of the interface and $\rho_i = \frac{1}{2}(\rho_{\mathrm{U}} + \rho_{\mathrm{L}})$ is the average of the upper and lower layer densities. To take advantage of symmetry, the level $z = 0$ is positioned at the mid-depth of the fluid, which has a total depth H. The intrusion can be viewed as a symmetric expansion of a surface- or bottom-propagating gravity current within an ambient of total depth $h_T = \frac{H}{2}$, as illustrated in Figure 2.2.

We first formulate the speed of a gravity current with density ρ_i moving in an ambient with density given by (2.1) for $0 \leq z \leq h_{\mathrm{T}} \equiv \frac{H}{2}$. Benjamin (1968) predicted that an energy conserving gravity current released from a lock of height h_{T} will propagate with a head height of $h_{\mathrm{T}}/2$ in a uniform ambient. Ungarish (2006) made an equivalent prediction for the propagation of a gravity current in a linearly stratified ambient. Here, it is also assumed that the head height is $h_{\mathrm{T}}/2$ and thus the the mean density over the depth of

the bottom-propagating gravity current is given by

$$\rho_{avg} = \begin{cases} \rho_{\mathrm{U}} + (\rho_i - \rho_{\mathrm{U}})\delta_h & 0 \le \delta_h \le 0.5 \\ \rho_i + \frac{\rho_{\mathrm{U}} - \rho_i}{4\delta_h} & 0.5 < \delta_h \le 1, \end{cases} \tag{2.2}$$

where $\delta_h \equiv \frac{h}{H}$. The gravity current speed, U_{gc}, given by Benjamin (1968) for a one-layer fluid and by Ungarish (2006) for a linearly stratified fluid is

$$U_{\mathrm{gc}} = \frac{1}{2}\sqrt{g\left(\frac{\rho_i - \rho_{avg}}{\rho_{00}}\right)h_{\mathrm{T}}}. \tag{2.3}$$

Here we have used the Boussinesq approximation allowing us to normalize the density difference by the characteristic density ρ_{00}.

By extension, the speed U_i of an intrusion moving along the interface of a stratified fluid with a density profile given by (2.1) is predicted by combining (2.2) and (2.3) and letting $h_{\mathrm{T}} = H/2$ to give

$$U_i = U_0 \begin{cases} (1 - \delta_h)^{1/2} & 0 \le \delta_h \le 0.5 \\ \frac{1}{2}\delta_h^{-1/2} & 0.5 < \delta_h \le 1, \end{cases} \tag{2.4}$$

where U_0 is the speed of a symmetric intrusion in a two-layer fluid ($\delta_h = 0$), given by

$$U_0 = \frac{1}{4}\sqrt{g'_{\mathrm{LU}}H}. \tag{2.5}$$

Here the reduced gravity between the upper and lower ambient fluid is

$$g'_{\mathrm{LU}} = g\left(\frac{\rho_{\mathrm{L}} - \rho_{\mathrm{U}}}{\rho_{00}}\right). \tag{2.6}$$

As illustrated by the dashed line in Figure 2.3, the intrusion speed is predicted to decrease as the relative thickness of the interface, δ_h, increases. This formula correctly predicts the rectilinear intrusion speed in the two-layer limit ($\delta_h \to 0$) and in the uniformly stratified limit ($\delta_h \to 1$).

2.2 Long small-amplitude waves at a thick interface

Symmetric intrusions may efficiently excite mode-2 solitary waves if they travel faster than long mode-2 interfacial waves at a thick interface. Rectilinear intru-
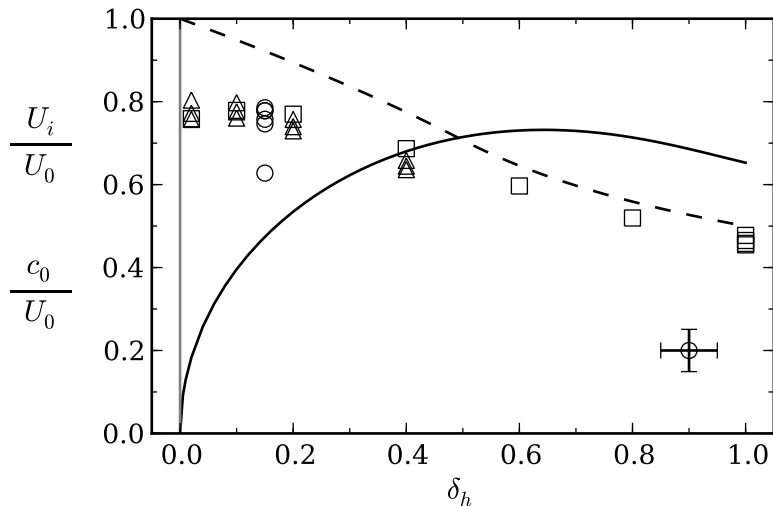
Figure 2.3: Relative initial intrusion speeds, U_i/U_0, computed numerically for ambients with piecewise-linear (squares) and hyperbolic tangent (triangles) profiles (discussed in Chapter 5) are compared to the predicted rectilinear speed (dashed line) defined by (2.4) and the relative speed, c_0/U_0, of a mode-2 linear long wave (solid line) defined by (2.20). Experimental speeds (discussed in Chapter 3) are plotted as circles with corresponding largest error bars shown in the lower right hand corner.

sion speeds were thus compared with long mode-2 waves in the x-z plane with a piecewise-constant three-layer density profile (Mehta et al., 2002; Sutherland and Nault, 2007). Here we find the speed of long axisymmetric interfacial waves in a three-layer fluid with piecewise-linear background density given by (2.1).

A cylindrical coordinate system is represented by a radial direction, r, an azimuthal direction, θ, and a vertical direction, z. In an axisymmetric system, derivatives with respect to θ are zero. Under this assumption, the fully nonlinear equations of motion for an inviscid, incompressible, Boussinesq

fluid are

$$\frac{\partial u}{\partial t} + u\frac{\partial u}{\partial r} + w\frac{\partial u}{\partial z} = -\frac{1}{\rho_{00}}\frac{\partial p}{\partial r}, \tag{2.7}$$

$$\frac{\partial w}{\partial t} + u\frac{\partial w}{\partial r} + w\frac{\partial w}{\partial z} = -\frac{1}{\rho_{00}}\frac{\partial p}{\partial z} - \frac{g}{\rho_{00}}\rho, \tag{2.8}$$

$$\frac{\partial \rho}{\partial t} + u\frac{\partial \rho}{\partial r} + w\frac{\partial \rho}{\partial z} + w\frac{\mathrm{d}\bar{\rho}}{\mathrm{d}z} = 0, \tag{2.9}$$

$$\frac{1}{r}\frac{\partial}{\partial r}(ru) + \frac{\partial w}{\partial z} = 0, \tag{2.10}$$

where equations (2.7) and (2.8) are the Euler equations which represent the conservation of momentum in the radial and vertical directions, respectively. The conservation of internal energy for a non-diffusive fluid is captured by (2.9), and the continuity equation for an incompressible fluid (2.10) ensures that mass is conserved. In the above equations, the radial and vertical components of the velocity field are given by u and w, respectively. The fluctuation pressure is represented by p and the fluctuation density is denoted by ρ. The background density is assumed to vary in the vertical as $\bar{\rho}(z)$ with its characteristic density denoted by ρ_{00}. The acceleration due to gravity is given by g.

In the study of small-amplitude waves, the nonlinear advection terms in equations (2.7)–(2.9) are neglected. From (2.10) we may introduce a stream function, ψ, such that

$$u = -\frac{\partial \psi}{\partial z} \quad \text{and} \quad w = \frac{1}{r}\frac{\partial}{\partial r}(r\psi). \tag{2.11}$$

Combining the coupled linear equations, a single governing equation in ψ can be obtained. This is a special case of the Taylor-Goldstein equation with no background flow. Explicitly, ψ satisfies

$$\frac{\partial^2}{\partial t^2}\left[\frac{1}{r}\frac{\partial}{\partial r}\left(r\frac{\partial \psi}{\partial r}\right) - \frac{\psi}{r^2} + \frac{\partial^2 \psi}{\partial z^2}\right] + N^2\left[\frac{1}{r}\frac{\partial}{\partial r}\left(r\frac{\partial \psi}{\partial r}\right) - \frac{\psi}{r^2}\right] = 0, \tag{2.12}$$

where

$$N^2 = -\frac{g}{\rho_{00}}\frac{\mathrm{d}\bar{\rho}}{\mathrm{d}z} \tag{2.13}$$

13

is the squared buoyancy frequency.

Using separation of variables, (2.12) can be solved to give bounded solutions of the streamfunction in the form

$$\psi(r, z, t) = A_\psi J_1(kr)\phi(z)e^{-i\omega t}, \tag{2.14}$$

where A_ψ is the amplitude, k is the radial wavenumber, ω is the wave frequency, J_1 is the first-order Bessel function of the first kind and ϕ is the vertical structure function which solves

$$\frac{\mathrm{d}^2\phi}{\mathrm{d}z^2} + k^2 \left(\frac{N^2}{\omega^2} - 1\right)\phi = 0. \tag{2.15}$$

The solution of this ordinary differential equation depends on the upper and lower boundary conditions as well as the stratification of the fluid prescribed through N^2.

In a fluid with a density profile given by (2.1) and no-normal-flow boundary conditions at $z = \pm\frac{H}{2}$, the vertical structure of a mode-2 wave satisfies

$$\phi(z) = \begin{cases} \frac{\sinh\left[k(\frac{H}{2}-z)\right]}{\sinh\left[\frac{k}{2}(H-h)\right]} & \frac{h}{2} < z < \frac{H}{2} \\ \frac{\sin(mz)}{\sin\left(\frac{mh}{2}\right)} & -\frac{h}{2} \leq z \leq \frac{h}{2} \\ -\frac{\sinh\left[k(\frac{H}{2}+z)\right]}{\sinh\left[\frac{k}{2}(H-h)\right]} & -\frac{H}{2} < z < -\frac{h}{2}. \end{cases} \tag{2.16}$$

Here the vertical wavenumber of the disturbance within the interface is

$$m = k\sqrt{N_0^2/\omega^2 - 1}, \tag{2.17}$$

in which the squared buoyancy frequency of the thick interface is

$$N_0^2 = \frac{g}{\rho_{00}}\frac{(\rho_{\mathrm{L}} - \rho_{\mathrm{U}})}{h}. \tag{2.18}$$

Using (2.17), k and ω are implicitly related by the dispersion relation

$$k\tan\left(\frac{mh}{2}\right) + m\tanh\left[\frac{k}{2}(H-h)\right] = 0. \tag{2.19}$$

In the long wave limit this becomes

$$\tan\left(\frac{N_0 h}{2c_0}\right) + \frac{N_0}{2c_0}(H - h) = 0, \tag{2.20}$$

where $c_0 = \omega/k$ is the long wave speed for a mode-2 wave. This speed is plotted by the solid line in Figure 2.3. The same result would be found for rectilinear interfacial waves. This indicates that although the radial structure of the waves is different, the long wave speed is the same.

Given that the interface has a finite thickness ($\delta_h > 0$), we expect that a mode-2 wave can be established by the widening of the interface. Furthermore, if the intrusion speed is supercritical ($U_i > c_0$) we expect the wave to take the form of a nonlinear solitary wave, whereas subcritical intrusions ($U_i < c_0$) generate linear waves. Whether, or not, the intrusion is supercritical can be prescribed by the value of the Froude number, $\text{Fr} \equiv U_i/c_0$. This is defined such that $\text{Fr} > 1$ corresponds to a supercritical intrusion from which solitary waves are expected to be generated. Comparing the solid and dashed lines in Figure 2.3, we expect that $\text{Fr} > 1$ if $\delta_h \lesssim 0.5$.

2.3 Internal Solitary Waves

KdV theory for rectilinear internal solitary waves is well-established (Benney, 1966). Using perturbation methods, Weidman and Velarde (1992) attempted to extend the theory to an axisymmetric geometry. However, the result was asymptotically inconsistent and it predicted an amplitude decrease as $r^{-2/3}$, inconsistent with energy conservation. Here, after reviewing rectilinear theory we present two alternate approaches, one rigorous and one heuristic, that are used to derive an energy conserving axisymmetric KdV equation.

2.3.1　Rectilinear KdV Theory

In a rectilinear geometry, internal solitary waves in a stratified fluid can be modelled by the KdV equation. The formulation by Benney (1966) predicts that in the Boussinesq approximation the vertical displacement field, ξ, has the form

$$\xi(x, z, t) = a(x, t)\phi(z), \tag{2.21}$$

in which $a(x, t) = a(x - ct)$ satisfies the KdV equation that includes the advection term:

$$a_t + c_0 a_x + \gamma a a_x + \beta a_{xxx} = 0. \tag{2.22}$$

Here the subscripts denote derivatives and the constants γ and β are given by (Benney, 1966)

$$\gamma = \frac{3}{2} c_0 \frac{\int_0^{\frac{H}{2}} \phi_z^3 \, dz}{\int_0^{\frac{H}{2}} \phi_z^2 \, dz} \qquad \text{and} \qquad \beta = \frac{1}{2} c_0 \frac{\int_0^{\frac{H}{2}} \phi^2 \, dz}{\int_0^{\frac{H}{2}} \phi_z^2 \, dz}, \tag{2.23}$$

where c_0 is the linear long wave speed. For a stratified ambient with the density profile given by (2.1), we exploit symmetry and consider only the upper half of the domain $(h_T = \frac{H}{2})$. The corresponding vertical structure function, ϕ, is given by the long wave limit of (2.16) with $0 \leq z \leq \frac{H}{2}$ and the long wave speed, c_0, satisfies (2.20).

The solution of (2.22), which assumes an isolated, steadily propagating disturbance is

$$a(x - ct) = a_0 \operatorname{sech}^2\left(\frac{x - ct}{\lambda}\right). \tag{2.24}$$

The speed, c, and width, λ, of the wave depend on the maximum displacement amplitude, a_0, by

$$c = c_0 + \frac{\gamma}{3} a_0 \qquad \text{and} \qquad \lambda^2 = \frac{12\beta}{\gamma} \frac{1}{a_0}. \tag{2.25}$$

The KdV coefficients, along with the wave speed and width, are shown in Figure 2.4 as functions of interface thickness.
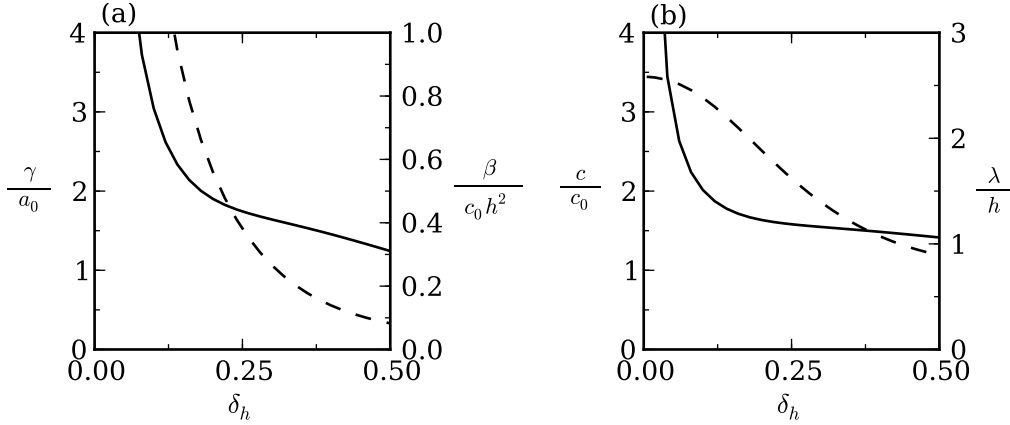
Figure 2.4: (a) Coefficients of the KdV equation as functions of interface thickness. The nonlinear coefficient, γ, is shown by the solid line and the dispersion coefficient, β, is shown by the dashed line. (b) The speed, c, (solid line) and width, λ, (dashed line) of a rectilinear solitary wave as a function of interface thickness.

From the numerical simulations, which are reported upon later, it is easier to diagnose the structure of the vertical velocity rather than the vertical displacement field. The vertical velocity derived from the vertical displacement field is

$$w(x,z,t) = \frac{\partial \xi}{\partial t} \simeq 2.598 A_w \operatorname{sech}^2\left(\frac{x-ct}{\lambda}\right)\tanh\left(\frac{x-ct}{\lambda}\right)\phi(z), \qquad (2.26)$$

in which the coefficient satisfies

$$\frac{2a_0 c}{\lambda} \simeq 2.598 A_w. \qquad (2.27)$$

Here A_w is defined as the maximum value of w. In these expressions, the value 2.598 is determined from the computed maximum value of $\operatorname{sech}^2(x)\tanh(x)$.

2.3.2 Axisymmetric KdV – Rigorous Derivation

Weidman and Velarde (1992) extended the theory of Benney (1966) to derive a formula for the leading order weakly nonlinear evolution of axisymmetric internal solitary waves. Here we outline a similar derivation but we further

17

impose that the amplitude of the wave must decrease as $r^{-1/2}$ as is required by energy conservation.

For an incompressible Boussinesq fluid, the governing equations of motion are given by (2.7) – (2.10). Putting the nonlinear terms on the right-hand side, the equations are

$$\rho_{00} u_t + p_r = -\rho_{00}(uu_r + wu_z), \tag{2.28}$$

$$p_z + \rho g = 0, \tag{2.29}$$

$$\rho_t + w\bar{\rho}\,' = -(u\rho_r + w\rho_z), \tag{2.30}$$

$$\frac{1}{r}(ru)_r + w_z = 0, \tag{2.31}$$

in which the subscripts denote partial derivatives. Because we are interested in long waves, it is assumed for now that the flow is hydrostatic. Therefore, the vertical momentum equation (2.8) is replaced by (2.29). In Eulerian coordinates, the vertical displacement field, ξ, is related at leading order to the velocity fields by

$$w - \xi_t \simeq \frac{1}{r}(r\xi u)_r. \tag{2.32}$$

The linear terms on the left-hand side of (2.28) – (2.32) can be combined to get a linear operator acting on ξ alone. The corresponding right-hand side of the resulting combined equation gives the nonlinear terms which non-negligibly perturb the displacement of moderately large amplitude waves.

To determine the weakly nonlinear evolution equation, the vertical displacement field is expanded in terms of the amplitude parameter, α, as follows:

$$\xi(r, z, t) = \alpha\xi_0 + \alpha^2\xi_1 + ... \tag{2.33}$$

The vertical structure of the leading order solution, ξ_0, is assumed to be separable from the slowly varying horizontal space and time dependence in the following way:

$$\xi_0 = \left(\frac{r_0}{r}\right)^{1/2} A(R, \tau)\phi(z). \tag{2.34}$$

18

Here $R = \epsilon(r - ct)$ is the translating radial co-ordinate which varies slowly as measured by ϵ. For consistency with the perturbation analysis that follows, the slow time scale is taken to be $\tau = \epsilon \alpha t$. Different from the axisymmetric theory of Weidman and Velarde (1992), here we have imposed energy conservation by requiring the magnitude of ξ_0 to decrease as $r^{-1/2}$ beyond some radius r_0. The vertical structure function, ϕ, and the amplitude, A, are both of order unity.

Inserting (2.33) and the corresponding expansions for $\vec{u}$, ρ and p into the governing equations (2.28) – (2.32), extracting leading order terms in α, and assuming r/r_0 is large gives

$$\mathcal{L}\xi_0 = 0, \tag{2.35}$$

where the linear operator $\mathcal{L}$ is defined as

$$\mathcal{L} \equiv c_0^2 \partial_{Rzz} + N^2 \partial_R, \tag{2.36}$$

in which $N^2(z)$ is the squared buoyancy frequency. Equations (2.35) and (2.36) result in the ordinary differential equation for the vertical structure function

$$c_0^2 \phi'' + N^2 \phi = 0. \tag{2.37}$$

In particular, for the piecewise-linear density profile given by (2.1), ϕ is given by the long-wave limit of (2.16); the vertical structure is the same whether in a rectilinear or cylindrical geometry.

At order α^2 and assuming $r \gg r_0$, the following equation is satisfied:

$$\mathcal{L}\xi_1 = \mathcal{N}, \tag{2.38}$$

where the nonlinear operator $\mathcal{N}$ is given in terms of the leading-order functions A and ϕ through

$$\mathcal{N} = 2c_0 \phi'' A_\tau + [\, 2c_0^2(\phi\phi')_{zz} + 2N^2\phi\phi'' + (N^2)_z\phi^2$$
$$+ 2c_0^2 \phi'\phi'' - c_0^2(\phi\phi'')_z \,] \left(\frac{r_0}{r}\right)^{1/2} A A_R. \tag{2.39}$$

Here the primes and z-subscripts both denote ordinary z-derivatives.

Recognizing (2.36) as a self-adjoint operator in z, both sides of (2.38) are multiplied by ξ_0 and the result is integrated over the domain height ($0 \leq z \leq h_T$). By construction, the left-hand side evaluates to zero, thus we arrive at the following approximate equation describing the influence of nonlinearity upon the amplitude A at large $r \gg r_0$:

$$A_\tau + \gamma \left(\frac{r_0}{r}\right)^{1/2} A A_R = 0. \tag{2.40}$$

Additionally including the effects of linear dispersion introduces the term βA_{RRR} on the left-hand side of (2.40). In the result, both γ and β are defined as for rectilinear waves by (2.23). The result can rewritten in terms of r, t and $a = \alpha \left(\frac{r_0}{r}\right)^{1/2} A$, as

$$a_t + c_0 \left(a_r + \frac{a}{2r}\right) + \gamma \left(a a_r + \frac{a^2}{2r}\right) + \beta a_{rrr} = 0. \tag{2.41}$$

Somewhat surprisingly, with the omission of the $a^2/2r$ term, this result is identical to that of Weidman and Velarde (1992). Furthermore, setting $\phi(z)$ to be the vertical structure function of surface waves in a one-layer fluid gives the formula derived by Miles (1978) for cylindrical solitary surface waves. However, as was pointed out by Weidman and Zakhem (1988) for the surface wave equation, the theory presented here is asymptotically inconsistent. By requiring $r \gg r_0$ in order to arrive at the KdV-like equation (2.41), the balance between nonlinear steepening and dispersion may no longer be valid. Furthermore, Weidman and Zakhem (1988) found that for large r, the solution of (2.41) satisfied $a \sim r^{-2/3}$, whereas energy conservation requires that the amplitude decreases with radius as $r^{-1/2}$.

2.3.3   Axisymmetric KdV − Heuristic Derivation

Because the rigorous attempt at deriving an axisymmetric KdV equation did not yield an energy conserving result, here we attempt to extend the rectilinear

theory to describe a solitary wave that spreads radially. For a solitary wave spreading as an expanding ring with sufficiently large radius, we may assume that the front on any point along the circumference negligibly feels the curvature of the front but that the amplitude nonetheless decreases with radius as $r^{-1/2}$. Thus, by extension of (2.26), we predict that the vertical velocity field should evolve as

$$w \simeq 2.598 A_{w0} \left(\frac{r_0}{r}\right)^{1/2} \mathrm{sech}^2 \left(\frac{r - ct}{\lambda}\right) \tanh \left(\frac{r - ct}{\lambda}\right) \phi(z), \qquad (2.42)$$

in which the amplitude A_{w0} is measured at a distance r_0 where the axisymmetric solitary wave is first generated.

For measured A_{w0}, we can use (2.25) and (2.27) to determine the initial displacement amplitude, a_0, the solitary wave speed, c, and the width, λ. As the wave spreads radially, $A_w = A_{w0}(r_0/r)^{1/2}$ decreases. Correspondingly, these equations predict that the displacement amplitude and speed should decrease and its width should increase. Eventually, the amplitude will be so small that weakly nonlinear effects associated with wave steepening will become negligible, so that linear dispersion dominates the evolution.

In contrast to the asymptotically inconsistent equation (2.41), the heuristic solution of the form (2.42) is established for $r \gtrsim r_0$. The corresponding vertical displacement field of the form $a(r, t) = a_0(r_0/r)^{1/2}\mathrm{sech}^2[(r - ct)/\lambda]$ does not satisfy (2.41). Instead, through manipulation of rectilinear KdV theory, it satisfies the leading-order equation

$$a_t + c_0 \left(a_r + \frac{a}{2r}\right) + \gamma \left(\frac{r}{r_0}\right)^{1/2} \left[aa_r + \frac{a^2}{2r}\right] + \beta a_{rrr} = 0. \qquad (2.43)$$

Compared to (2.41), here the nonlinear term is of order $(r/r_0)^{1/2}$, which seems to suggest that the balance between nonlinearity and dispersion exists for large r. However, because $a \propto r^{-1/2}$ the nonlinear term will eventually become negligible as the wave moves to large r and the motion will then be governed

by

$$a_t + c_0 \left(a_r + \frac{a}{2r} \right) + \beta a_{rrr} = 0. \qquad (2.44)$$

This equation simply describes a dispersing linear wave. Using the method of stationary phase, it can be shown that the dispersion results in spreading such that the amplitude decreases as $r^{-1/2}$. Together with the effect of geometrical spreading, the amplitude of a long wave thus decreases as r^{-1}.

Through comparison of these theories with the results of numerical simulations (Chapter 5), we will show that the heuristic solution (2.42) more accurately represents the life-cycle of axisymmetric solitary waves generated by intrusions. Thus we show that the admittedly inconsistently derived cylindrical solitary wave equation of Weidman and Velarde (1992) and our extension of it in Section 2.3.2, indeed provide an inaccurate description of axisymmetric solitary waves. However it must be emphasized that (2.43) is heuristic: whereas the balance in rectilinear KdV theory for a disturbance of length L is $aL^2 \sim 1$, the nonlinear dispersive 'balance' is $aL^2 \sim r^{-1/2}$. And so the nature of competition between nonlinearity and dispersion changes with radial distance.

Chapter 3

Experiments

The motivation for this work was largely based on the experiments of axisymmetric intrusions that were conducted, but not analysed, by Joshua Nault and Lauren Blackburn in 2003 and 2004, respectively. I did conduct some experiments myself, although the results are not presented here. This chapter reports primarily upon the analysis methodology and the quantitative results.

3.1 Set-up

Experiments were conducted in a cylindrical acrylic tank with an inner diameter of $2R = 90.7$ cm and a height of 30.0 cm as illustrated in Figure 3.1. The tank was filled to a depth of 5 cm with salt water of density ρ_{L}. Using a sponge float, fresh water of density ρ_{U} was added to the surface until the total depth of the fluid was $H = 10$ cm. In all experiments, the density of the upper layer was $\rho_{\mathrm{U}} = 0.9982$ g/cm^3, whereas the lower layer density varied between $\rho_{\mathrm{L}} = 1.0515$ g/cm^3 and $\rho_{\mathrm{L}} = 1.1047$ g/cm^3. Due to mixing and diffusion during the filling process, the interface between the two layers was assumed to vary smoothly over a depth of $h = 1.5 \pm 0.5$ cm.

A small acrylic cylindrical lock with an inner diameter of $2r_0 = 12$ cm and a height of 22.8 cm was inserted at the centre of the tank. The fluid within the lock was then dyed and vigorously mixed, so that its density, ρ_i, was equal to
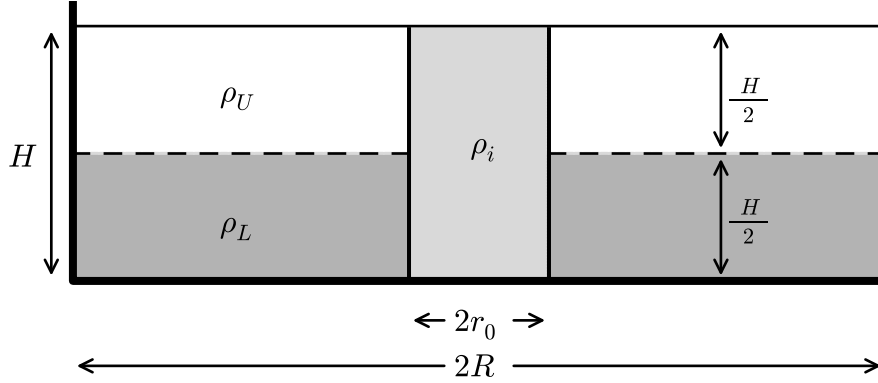
Figure 3.1: A side-view schematic of the experimental setup used to observe intrusions propagating in a cylindrical tank. Although the ambient fluid is shown here as two distinct layers, it was assumed that the filling process and diffusion caused the interface to have a thickness of approximately 1.5 ± 0.5 cm. For all experiments, the density of the fluid within the lock was $\rho_i = \frac{1}{2}(\rho_{\mathrm{U}}+\rho_{\mathrm{L}})$.

the mean density of the ambient fluid. The small concentration of dye allowed the intrusion to be visualized without significantly changing the density of the fluid in the lock.

Using a string and pulley system, the cylindrical lock was rapidly lifted vertically out of the tank. This caused an intrusion to propagate outwards along the interface between the light and dense fluid. An experiment was considered successful if the lock removal was purely vertical causing the intrusion to propagate axisymmetrically.

3.2   Analysis and Results

Figures 3.2(a) and (b) show an overhead view taken from a COHU CCD camera situated 2 m above the tank. These snapshots were taken at $t = 2$ s and 4 s after the lock was removed. The circular spreading of dyed fluid indicates that the intrusion propagates axisymmetrically and the linear diagonal contour in the time series (Figure 3.2c) confirms that it does so at a constant rate. At about $t = 6$ s, the intrusion reflects off the cylinder side wall at $R \simeq 45$ cm

24

and then returns to the centre of the tank at approximately the same speed.

The magnitude of the speed was determined by measuring the slopes of two diagonal contours from time series images. These measurements were typically made between $r = 12$ cm and $r = 24$ cm (i.e. between one to three lock-radii from the edge of the lock). The intrusion speed, U_i, was then calculated as the average of the four slope values. The experimental error was taken to be the standard deviation in the slopes.

3.3 Discussion

The measured speeds in six experiments are plotted as solid circles in Figure 2.3. In the figure, the speeds are non-dimensionalised by U_0, given by (2.5). For all experiments, the interface thickness was taken to be $h = 1.5(\pm 0.5)$ cm; therefore, with $H = 10$ cm, $\delta_h = 0.15(\pm 0.05)$. With the exception of one experiment, Figure 2.3 shows that within error the measured speeds collapse to a value of $0.75(\pm 0.06)U_0$. This suggests that axisymmetric intrusions are slower than rectilinear intrusions which, for $\delta_h = 0.15$, have a predicted speed of $U_i/U_0 \approx 0.92$ by (2.4). Furthermore, the measurements are consistent with axisymmetric gravity current experiments (Huppert and Simpson, 1980; Patterson et al., 2006) and simulations (Zhang et al., 2010), in which the observed front speeds were about $0.8U_{\mathrm{gc}}$. Here U_{gc}, given by (2.3), plays the role of U_0 for gravity currents.

The experiments that are presented here were all vertically symmetric, meaning that the depths of the upper and lower layers were equal and the density of the intruding fluid was equal to the average density of the ambient (ie. $\rho_i = \frac{1}{2}(\rho_{\mathrm{U}} + \rho_{\mathrm{L}})$). In all six experiments, the intrusions propagated to the tank wall at a constant speed, a distance of $6.5r_0$ from the edge of the lock. As explained in Section 1.2.2, axisymmetric gravity currents are expected to decelerate around $3r_0$ from the release location, a consequence
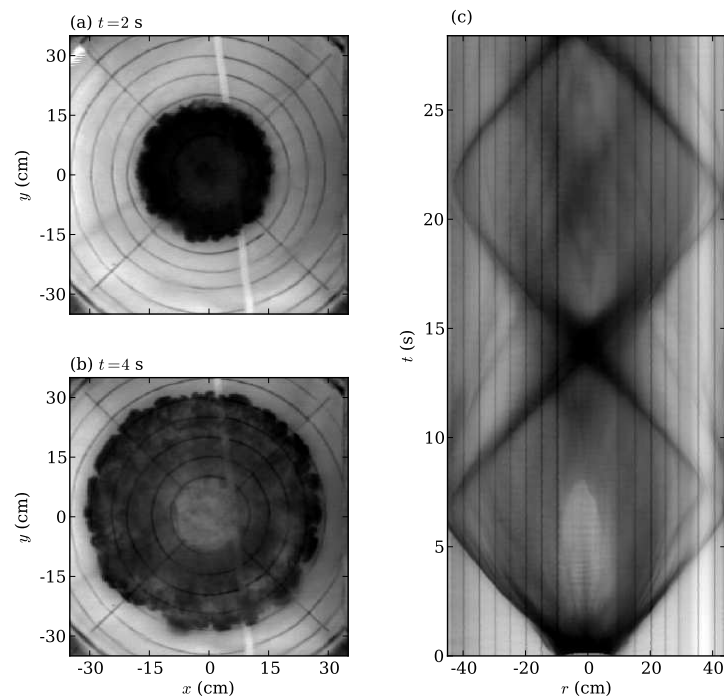
Figure 3.2: Top view images at (a) $t = 2\,\text{s}$ and (b) $t = 4\,\text{s}$. (c) Time series of an axisymmetric intrusion where the ambient density difference is $\rho_L - \rho_U = 0.1065\ \text{g/cm}^3$. The lock fluid is darkly dyed. The diamond pattern in the time series indicates that the intrusion moves at a constant speed radially away from the lock and also radially inward after reflection from the side walls.

of their decreasing head height, but this does not happen in the vertically symmetric intrusion experiments. Instead they propagate at a constant speed beyond 8 lock radii. It is therefore hypothesized that the vertical symmetry of the experiments presented here allows the intrusion efficiently to excite a double-humped mode-2 wave at the density interface of the ambient fluid, which then carries the intrusion outwards at a constant speed. Because the experiment analysis was limited to top-view camera images, it was necessary to use numerical simulations to confirm the existence of these waves and to examine their properties.

Chapter 4

Numerical Simulations

Fully nonlinear numerical simulations were performed to confirm the experimental results presented in Chapter 3, as well as to obtain a better understanding of internal solitary waves in an axisymmetric geometry. The original finite-difference code was created by Richard Rotunno for the purpose of studying hurricanes. Preliminary modifications were made by Bruce Sutherland to employ the Boussinesq approximation and to advect the density field as opposed to the potential temperature field. I was responsible for debugging the code, adding a passive tracer field, and including a sponge layer for enhanced stability. I also tested the code by simulating a mode-1 small-amplitude wave in a linearly stratified fluid. As the wave evolved, the simulated fields and frequencies were compared to the respective analytical predictions (not shown). This chapter presents a general overview of the solution method with emphasis on features relevant to the applications discussed in the chapters that follow.

4.1 Governing Equations

In Section 2.2 the governing equations for an incompressible, inviscid, Boussinesq fluid were given for an axisymmetric geometry. In the numerical code, the effects of viscosity and diffusion are included to ensure stability by damping out numerical noise. In addition, the code includes the effects of rotation

and azimuthal flow, although these dynamics were not included in the simulations discussed in Chapters 5 and 6. Requiring no variation in the azimuthal direction, the governing equations are

$$\frac{\partial u}{\partial t} + u\frac{\partial u}{\partial r} + w\frac{\partial u}{\partial z} - \frac{v^2}{r} - fv = -\frac{1}{\rho_{00}}\frac{\partial p}{\partial r} + \nu\left[\nabla^2 u - \frac{u}{r^2}\right], \qquad (4.1)$$

$$\frac{\partial v}{\partial t} + u\frac{\partial v}{\partial r} + w\frac{\partial v}{\partial z} + \frac{uv}{r} + fu = \nu\left[\nabla^2 v - \frac{v}{r^2}\right], \qquad (4.2)$$

$$\frac{\partial w}{\partial t} + u\frac{\partial w}{\partial r} + w\frac{\partial w}{\partial z} = -\frac{1}{\rho_{00}}\frac{\partial p}{\partial z} - \frac{\rho g}{\rho_{00}} + \nu\nabla^2 w, \qquad (4.3)$$

$$\frac{\partial \rho}{\partial t} + u\frac{\partial \rho}{\partial r} + w\frac{\partial \rho}{\partial z} + w\frac{\mathrm{d}\bar{\rho}}{\mathrm{d}z} = \kappa\nabla^2\rho, \qquad (4.4)$$

$$\frac{1}{r}\frac{\partial}{\partial r}(ru) + \frac{\partial w}{\partial z} = 0, \qquad (4.5)$$

where v is the azimuthal velocity, f is the rotation rate, ν is the viscosity and κ is the diffusivity. The remaining variables are the same as those in (2.7) – (2.10) and are described below those equations in Section 2.2. In an axisymmetric geometry the Laplacian is given by

$$\nabla^2 = \frac{1}{r}\frac{\partial}{\partial r}\left(r\frac{\partial}{\partial r}\right) + \frac{\partial^2}{\partial z^2}. \qquad (4.6)$$

By introducing the azimuthal vorticity,

$$\zeta = \frac{\partial u}{\partial z} - \frac{\partial w}{\partial r}, \qquad (4.7)$$

and using equation (4.5), the pressure can be eliminated from equations (4.1) and (4.3) to yield

$$\frac{\partial \zeta}{\partial t} + ur\frac{\partial}{\partial r}\left(\frac{\zeta}{r}\right) + w\frac{\partial \zeta}{\partial z} - \frac{1}{r}\frac{\partial}{\partial z}\left(fvr + v^2\right) = \frac{g}{\rho_{00}}\frac{\partial \rho}{\partial r} + \nu\left(\nabla^2\zeta - \frac{\zeta}{r^2}\right). \ (4.8)$$

The numerical code that was used in the completion of this work solves the coupled partial differential equations for the azimuthal velocity (4.2), perturbation density (4.4), and vorticity (4.8).

The streamfunction is related implicitly to the vorticity field by

$$\nabla^2\psi - \frac{\psi}{r^2} = -\zeta. \qquad (4.9)$$

29
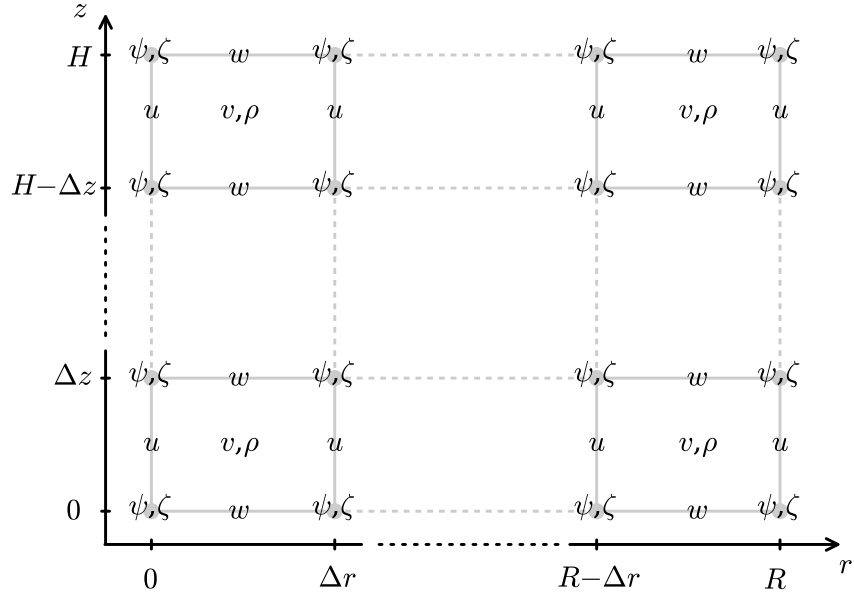
Figure 4.1: A graphical representation of the discretization of the staggered grid.

Inverting this equation gives ψ from ζ and, using (2.11), this gives u and w.

A passive tracer is also advected and its concentration, C_{PT}, is governed by

$$\frac{\partial C_{\mathrm{PT}}}{\partial t} + u\frac{\partial C_{\mathrm{PT}}}{\partial r} + w\frac{\partial C_{\mathrm{PT}}}{\partial z} = \kappa_{\mathrm{PT}}\nabla^2 C_{\mathrm{PT}}, \tag{4.10}$$

where κ_{PT} represents a small diffusivity required for maintaining a smooth field.

4.2 Solution Method

For a simulation, the domain is specified by its radial extent, R, and its vertical extent, H. It is then discretized into a uniform grid consisting of N_r points in the radial direction and N_z points in the vertical direction.

The grid is 'staggered' such that the fields are not all computed at the same locations in the domain. This is illustrated pictorially in Figure 4.1. The v and ρ fields are approximated at the centres of the grid boxes, whereas the ζ

30

and ψ fields are approximated at each node. Furthermore, the radial velocity, u, is computed at node locations in the radial direction and at midpoint locations in the vertical direction. The vertical velocity, w, is computed at the node locations in the vertical direction and at midpoint locations in the radial direction.

At each instant in time, (4.9) is inverted using a Fourier-Bessel series. Explicitly, the spatial components of the vorticity field are represented by

$$\zeta(r, z) = \sum_{i=1}^{N_r/2} \sum_{j=1}^{N_z} A_\zeta(k_i, m_j) J_1(k_i r) \sin(m_j z), \tag{4.11}$$

where $k_i = \alpha_i/R$ is the radial wave number given in terms of the zeros, α_i, of the $J_1(r)$ Bessel function and the vertical wave number is given by $m_j = 2\pi j/H$. The series coefficients, A_ζ, are found from the inverse Fourier-Bessel transform of ζ. Likewise, we may assume the streamfunction takes the form

$$\psi(r, z) = \sum_{i=1}^{N_r/2} \sum_{j=1}^{N_z} A_\psi(k_i, m_j) J_1(k_i r) \sin(m_j z). \tag{4.12}$$

Substituting the series expansions for ζ and ψ into (4.9) and comparing terms gives a sequence of simple algebraic formulae relating A_ψ to the computed values of A_ζ. Finally, (4.12) can be used to reconstruct $\psi(r, z)$.

Representing ψ as a J_1 function in r and a sine function in z ensures that the no-normal flow condition, $\mathbf{u} \cdot \hat{\mathbf{n}} = 0$, is satisfied at the free-slip boundaries. Additionally, the form of (4.11) constrains ζ to be zero at all boundaries. This assumption is suitable for the study of flows which, near the boundary, are of uniform-density and inviscid (hence irrotational).

From the calculated ψ field, u and w are computed using (2.11). Then, the spatial derivatives in (4.2), (4.4), (4.8) and (4.10) are approximated using second-order finite difference methods.

The evolution equations are then stepped forward in time using a leap-frog scheme that is second-order accurate. More specifically, each field is advanced

as

$$F(t_{n+1}) = F(t_{n-1}) + 2\frac{\partial F(t_{n^*})}{\partial t}\Delta t, \tag{4.13}$$

where Δt is the time-step, F represents v, ρ, ζ or C_{PT} and $\partial_t F$ is given by the spatial derivatives in the Navier Stokes equations. For computational stability, the advection and forcing terms are calculated using fields at centred timesteps $(n^* = n)$, whereas the dissipation terms are calculated using fields evaluated a timestep earlier $(n^* = n - 1)$. Every 20 timesteps, the fields from the current and previous timestep are averaged. This is known as an Euler backstep and its purpose is to minimize time-splitting errors that occur in the leapfrog scheme.

4.3 Running the Code

For all the simulations presented in this work, intrusions were launched by a constant-volume lock-release. The code was initialized by specifying the lock radius, r_0, as well as the spatial resolution parameters $(N_r,\ N_z,\ R$ and $H)$. Typical values for $\Delta z = H/N_z$ and $\Delta r = R/N_r$ were 0.039 cm and 0.044 cm, respectively, for the idealized intrusion simulations presented in Chapter 5. The corresponding typical values for the river plume simulations presented in Chapter 6 were 1.6 m and 2.0 m. Typical values of the timestep (Δt) were 0.00125 s and 0.25 s for the intrusion and river plume simulations, respectively.

Input files were used to specify the background density field, $\bar{\rho}(z)$, and the initial ρ, v and C_{PT} fields. It was assumed there was no motion in the radial and vertical directions. Therefore u, w and ζ were initially set to zero.

To prevent the code from becoming numerically unstable while maintaining a reasonable computation speed, a sponge layer was included to damp out small-scale noise created by the collapse of the lock fluid. A spatially varying

Parameter	Intrusions	River Plumes
r_0	6 cm	2500 m
r_{in}	12 cm	2700 m
r_{out}	18 cm	3200 m
ν_{in}	0.1 cm²/s	$0.10 - 0.45$ m²/s
ν_{out}	0.01 cm²/s	$0.02 - 0.09$ m²/s

Table 4.1: The parameters used for the sponge layers in the simulations of vertically symmetric intrusions (Chapter 5) and river plumes (Chapter 6). The lock radius, r_0, is also given.

piecewise-linear viscosity was prescribed such that

$$\nu(r) = \begin{cases} \nu_{\mathrm{in}} & 0 \leq r \leq r_{\mathrm{in}} \\ \nu_{\mathrm{out}} - \left(\frac{\nu_{\mathrm{in}} - \nu_{\mathrm{out}}}{r_{\mathrm{out}} - r_{\mathrm{in}}} \right) (r - r_{\mathrm{out}}) & r_{\mathrm{in}} < r < r_{\mathrm{out}} \\ \nu_{\mathrm{out}} & r_{\mathrm{out}} \leq r \leq R, \end{cases} \tag{4.14}$$

where ν_{in} and ν_{out} are constants satisfying $\nu_{\mathrm{in}} > \nu_{\mathrm{out}}$. Typical values of r_{in} and r_{out} and the viscosities are given in Table 4.1. It should be noted, that in the river plume simulations the value of ν_{out} was up to 1000 times greater than physical value of 0.01 cm²/s. This was done to maintain numerical stability and it did not affect the motion at early times.

The code also requires the user to specify the values of ρ_{00}, g, κ and κ_{PT}. Because the code works with dimensional quantities, it is important that the units of these constants are consistent. For all simulations, $\rho_{00} = 1.00$ g/cm³ and $g = 980.6$ cm/s². The diffusivities, on the other hand, were treated differently for the intrusion and river plume simulations. For the intrusion simulations, κ and κ_{PT} were set to be everywhere equal to ν and therefore varied with r. For the river plume simulations, κ and κ_{PT} were constant throughout the domain and were given values such that the Schmidt number, $Sc = \nu_{\mathrm{out}}/\kappa$, was equal to 10.

As the simulations proceeded, snapshots of the density, vorticity, velocity and passive tracer fields were output at intervals of 0.1 s and 10 s for the

intrusion and river plume simulations, respectively.

All the simulations described in Chapters 5 and 6 were completed on the WestGrid High Performance Computing cluster, including the SGI Origin model 350 (8 MIPS, 700 MHz) and the SGI Altix XE320 model (2.5 GHz). Because the Fourier-Bessel transform is computationally expensive, the simulations described in this work required several days to complete. More specifically, simulations of idealized intrusions evolving over 14 s required about 36 hours of computing time. Simulations of river plumes evolving over 4000 s required at least 8 days.

Chapter 5

Axisymmetric Vertically Symmetric Intrusions

Fully nonlinear numerical simulations were performed to examine vertically symmetric intrusions and internal solitary waves in an axisymmetric geometry (McMillan and Sutherland, 2010). More specifically, the effect of a finite thickness interface was analysed. The results were compared to the theory presented in Chapter 2 and the experiments presented in Chapter 3.

5.1 Initial Conditions

The simulations were completed using the code described in Chapter 4 on a domain with a radius of $R = 45$ cm and a height of $H = 10$ cm. The grid consisted of $N_r = 1024$ radial points and $N_z = 256$ vertical points. To examine the long-time evolution of the system, simulations with a domain radius of $R = 80$ cm were also performed. The other input values are given in Section 4.3. It should be noted that the viscosity near the lock was 10 times greater than the physical value of 0.01 cm^2/s. The dynamics of the flow were unaffected using this viscosity because the Reynolds numbers were on the order of 10^3 indicating that viscosity did not govern the dominant motion. To confirm this, a high resolution simulation with a uniform viscosity of 0.01 cm^2/s was performed (this taking many days rather than many hours

to run) and it was found that the propagation and speed of the intrusion near the lock remained unchanged. The diffusivity of salt water, κ, was set to be everywhere equal to ν, even though its physical value is 10^{-5} cm^2/s. The purpose of doing this was again for numerical stability. However, the value of κ was still small enough that molecular diffusion had a negligible influence on the flow.

The simulations were completed for a non-rotating system with no background azimuthal flow. Therefore, $f = 0$ and $v = 0$. The code was initialized by a density field that mimicked the initial density of the experimental setup described in Chapter 3. Explicitly, we prescribed

$$\rho_{\text{init}}(r, z) = \begin{cases} \rho_i & 0 < r < r_0 \\ \bar{\rho}(z) & r_0 < r < R. \end{cases} \tag{5.1}$$

where $r_0 = 6$ cm is the radius of the lock. Simulations were completed with both a piecewise-linear background density, $\bar{\rho}(z)$, given by (2.1) and a smooth hyperbolic tangent profile given by,

$$\bar{\rho}_t(z) = \rho_i - \frac{1}{2}(\rho_{\text{L}} - \rho_{\text{U}}) \tanh\left(\frac{2z}{\delta_h H}\right). \tag{5.2}$$

For all simulations, the density within the lock was the average ambient density, $\rho_i = \frac{1}{2}(\rho_{\text{L}} + \rho_{\text{U}})$. The concentration of the passive tracer field, C_{PT}, was initially set to unity over $0 < r < r_0$ and zero elsewhere.

Simulations were performed with interface thicknesses of $\delta_h = 0.02$, 0.1, 0.2, 0.4, 0.6, 0.8 and 1.0 for $\bar{\rho}(z)$ given by (2.1) and $\delta_h = 0.02$, 0.1, 0.2 and 0.4 for $\bar{\rho}_t(z)$ given by (5.2). All simulations were completed with an upper layer density of $\rho_{\text{U}} = 0.9982$ g/cm^3. In different simulations, the lower layer density was set to $\rho_{\text{L}} = 1.0515$ g/cm^3, 1.0662 g/cm^3 and 1.1047 g/cm^3.

5.2   Results

In agreement with the experimental observations described in Chapter 3, axisymmetric intrusions at a thin interface ($\delta_h \leq 0.2$) were observed to propa-

gate beyond $8r_0$ at a constant speed as shown in Figure 5.1. On the contrary, axisymmetric bottom propagating gravity currents have been observed to decelerate as early as $3r_0$ from the edge of the lock (Huppert and Simpson, 1980; Patterson et al., 2006; Sutherland and Nault, 2007). Therefore, it is believed that the stratification of the thin interface allows for the formation of a nonlinear wave that tightly encloses the intrusion and advects it at a constant speed far from the lock.

This behaviour is evident in the sideview snapshots in Figure 5.2 for a simulation with an ambient density given by (5.2) with an interface thickness of $\delta_h = 0.2$. The wave and intrusion initially propagate outwards together, but some lock fluid leaks rearward of the intrusion and eventually, the intrusion head runs out of fluid. It then decelerates to a stop at $r = 8r_0$ while the wave continues to spread radially outwards.

This behaviour can be compared to the snapshots in Figure 5.3 for a simulation of an intrusion in a linearly stratified ambient. Again the intrusion excites a mode-2 wave. However, the wave is smaller in amplitude and the lock fluid is not tightly enclosed by the wave. The wave in this case is linear, and therefore, it is unable to transport the intruding fluid. Correspondingly, the intrusion decelerates after propagating a distance of 3 lock radii (at $r = 4r_0$), not unlike the gravity current observations. As shown in Figure 5.1, this deceleration and ultimate separation of intrusion and wave, was observed to occur at smaller r/r_0 for increasing δ_h.

For a range of simulations, the initial intrusion speeds, U_i, were measured by calculating the slope, dr_i/dt, for $2r_0 \leq r_i \leq 3r_0$. These speeds are plotted as squares and triangles in Figure 2.3 for intrusions in ambients with both piecewise-linear and hyperbolic tangent profiles. The results were found to be in good agreement with the speeds measured in laboratory experiments (open circles). Consistent with the rectilinear theory outlined in Section 2.1, as the
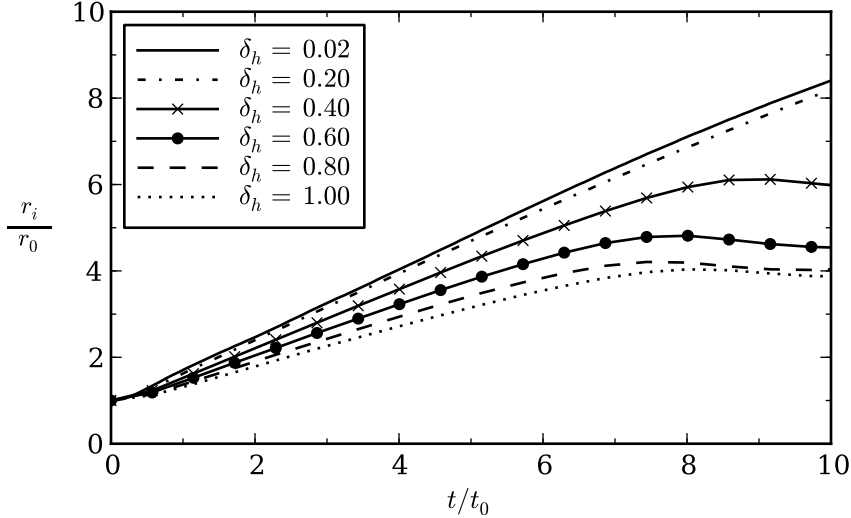
Figure 5.1: The location of the intrusion front versus time for simulations with $\rho_L = 1.0530$ g/cm^3 and $\bar{\rho}(z)$ given by (2.1). At a thick interface ($\delta_h \geq 0.60$), the intrusion begins to decelerate around $3r_0$, whereas at a thin interface ($\delta_h \leq 0.2$) the intrusion maintains a constant speed beyond $8r_0$.

thickness of the interface increases, the intrusion speed decreases. However, for all δ_h, axisymmetric intrusions were found to travel more slowly than the predicted speed of intrusions in a rectilinear geometry, given by (2.4). This implies that the curvature of the geometry has an effect on the initial intrusion speed.

Figure 2.3 also shows that compared to the long-wave speed, symmetric intrusions travel more quickly if $\delta_h \lesssim 0.4$ and hence the intrusion is supercritical. This observation provides further evidence that at a sufficiently thin interface the wave is nonlinear upon generation. Because nonlinear waves can transport mass, intrusions in ambients with $\delta_h \lesssim 0.4$ can be carried beyond 3 lock radii at a constant speed, consistent with the results presented in Figure 5.1. On the other hand, intrusions at thicker interfaces ($\delta_h > 0.4$) are subcritical and hence they excite linear waves, which are unable to transport mass.

Because the motivation of this work was to understand axisymmetric in-
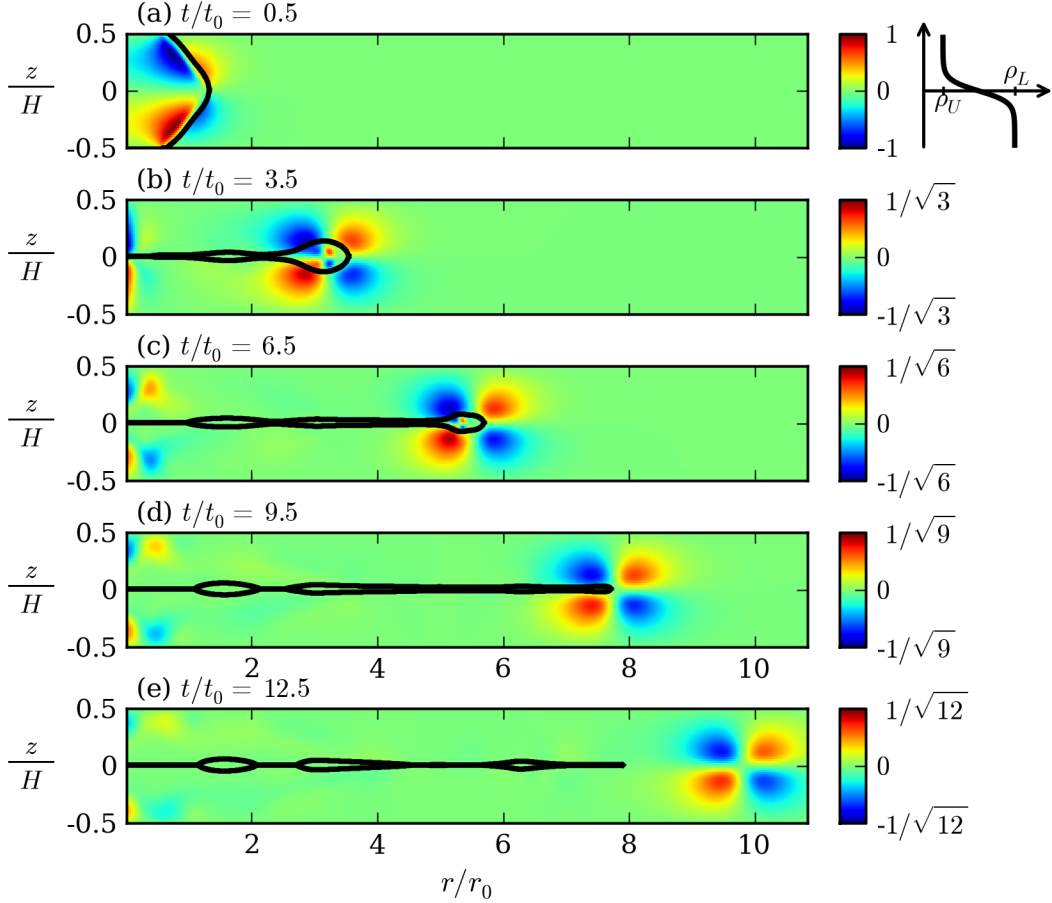
Figure 5.2: Snapshots of the normalized vertical velocity field, w/w_{max}, obtained from a numerical simulation of an axisymmetric intrusion in an ambient fluid with a background density, $\bar{\rho}_t$, given by Eq. (5.2) with a non-dimensional interface thickness of $\delta_h = 0.2$. The thick black lines outline the intrusion profile at each time and illustrate that the intrusion head is being carried outward by a wave. In each plot, the vertical velocity field is normalized by the maximum amplitude of the wave at $t/t_0 = 0.5$, where $t_0 = r_0/U_0$. The colourbar limits are scaled by $\sqrt{t/t_0 - 0.5}$, making it evident that the amplitude of the wave decays from its maximum value as $t^{-1/2}$. The wave is observed to propagate at a constant speed (ie. $r \sim t$); therefore, the amplitude of the wave is decreasing as $r^{-1/2}$ as is predicted by linear theory.
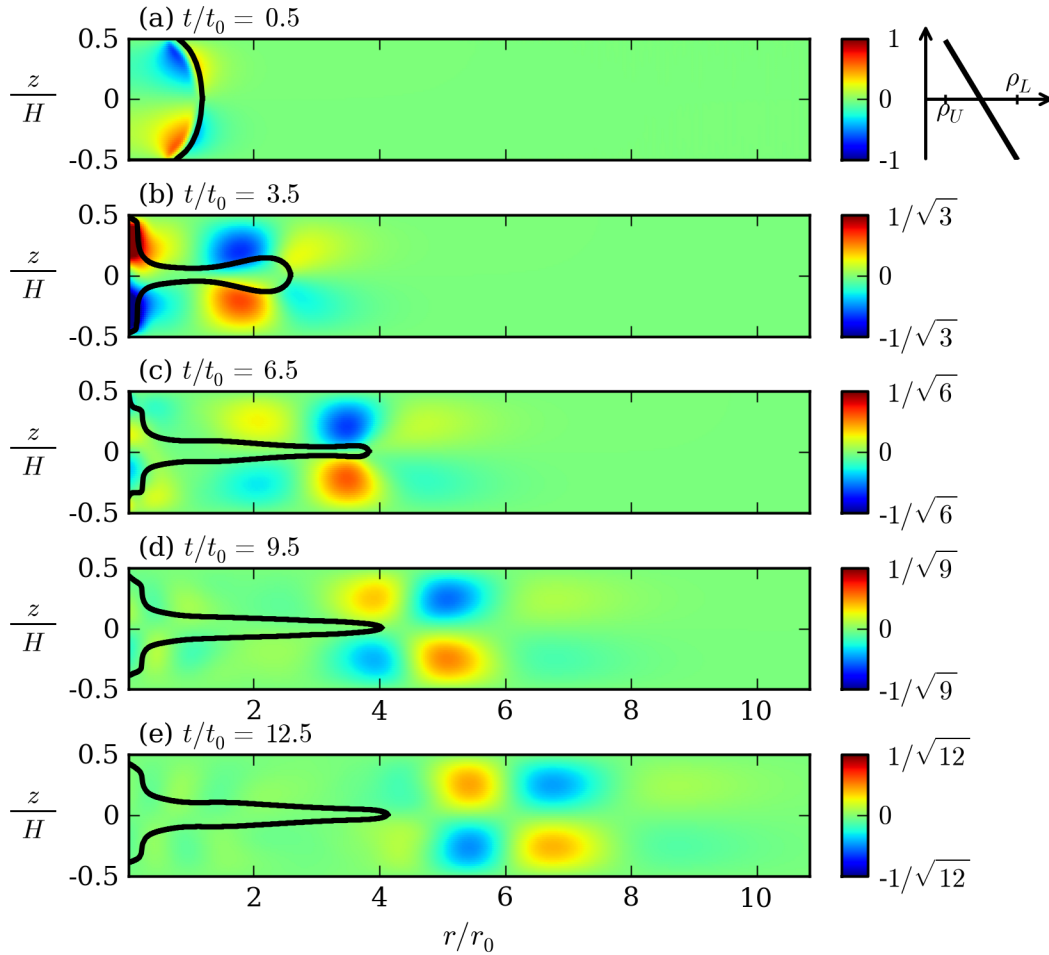
Figure 5.3: Snapshots of the normalized vertical velocity field obtained from a numerical simulation of an axisymmetric intrusion in an ambient fluid with a linearly stratified background density. The colorbars are the same as those in Figure 5.2 to illustrate that the magnitude of the wave is smaller in this ambient fluid. Futhermore, the generated waves move much slower and the intrusion fluid is not trapped, as in Figure 5.2.

ternal solitary waves, the properties of the nonlinear waves were measured for simulations where $\delta_h \leq 0.4$. Here, we present the results for the simulation with $\delta_h = 0.2$ that is shown in Figure 5.2.

To determine the wave's position, r_w, and amplitude, A_w, a radial time series (not shown) of the vertical velocity field was made by taking a radial slice at a height of $z/H = 0.15$. The wave's position was taken to be the location of maximum isopycnal displacement. As shown in Figure 5.4, $r_w \sim t$, indicating that the wave travelled at a constant speed throughout the simulation even after it separated from the intrusion front.

To ignore interactions of the wave with the intrusion, the amplitude of the leading wave crest was measured. The analysis of amplitude versus radial position, which is plotted in Figure 5.4, shows that the wave amplitude initially decays as $r_w^{-1/2}$. This behaviour is anticipated on the basis of energy conservation for a non-dispersive wave. Beyond $8r_0$, the wave separates from the intrusion and its amplitude becomes sufficiently small that linear dispersion increases the amplitude decay rate to r_w^{-1}. This late-time behaviour is consistent with the additional effects of linear dispersion on a small amplitude wave as discussed in Section 2.3.

The wave evolution was compared to the theory predicting its structure, which was presented in Section 2.3. To do this required first estimating the height, $h/2$, of the theoretical interface. Because the simulation had a continuously stratified ambient, $\bar{\rho}_t$, given by (5.2), the height at which the vertical velocity was a maximum ($z/H \simeq 0.15$) was assumed to correspond to $z = h/2$, where the normalized streamfunction amplitude satisfies $\phi(z) = 1$. Radial slices of the vertical velocity field were then taken at several times, as shown in Figure 5.5(a). For each slice, the maximum amplitude, A_w, was determined and equations (2.25) and (2.27) were solved for a_0, c and λ.

As shown in Figure 5.5(b), the profiles collapse onto a theoretical curve
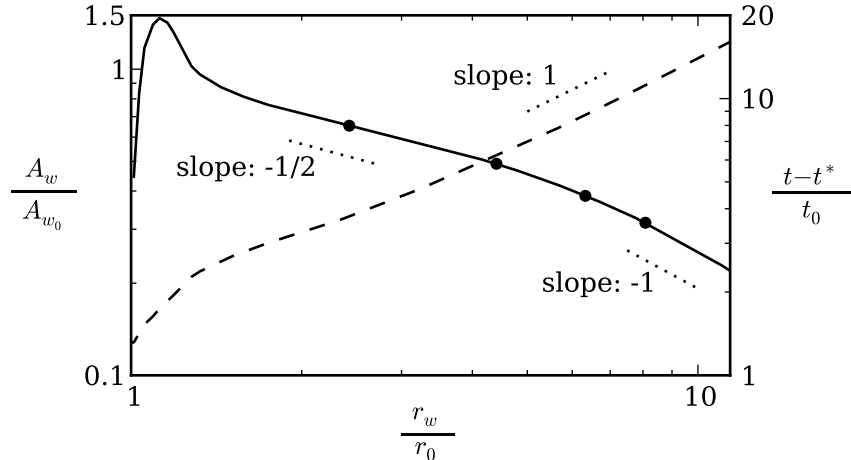
Figure 5.4: The wave amplitude and position for the simulation shown in Figure 5.2 with $\delta_h = 0.2$. The solid line shows the amplitude of vertical velocity, A_w, versus radial position, r_w, for the wave at a height of $z/H = 0.15$. A reference amplitude, A_{w_0}, is defined such that $A_w = A_{w_0}(r_w/r_0)^{-0.48}$ for $2r_0 \leq r_w \leq 3r_0$. The circles correspond to $t/t_0 = 2.5, 5.0, 7.5$ and 10.0, for which wave profiles are illustrated in Fig. 5.5. The radial position of the wave versus time is indicated by the dashed line. A reference time, t^*, is defined such that $r_w = \frac{\mathrm{d}r_w}{\mathrm{d}t}(t - t^*)$ for $4r_0 \leq r_w \leq 10r_0$. The curves are compared with lines of constant slope as indicated.

when the amplitude is scaled by $r_w^{-1/2}$ and the radial extent is shifted by $2r_0 + c\Delta t$ and scaled by λ. It should be noted that the reference location of $2r_0$ was chosen to ignore the initial generation of the wave caused by the intrusion. For the intermediate times, $t/t_0 = 5.0$ and 7.5, the simulation results are in excellent agreement with the theory. However, at $t/t_0 = 10.0$, the wave amplitude became small and linear dispersion slightly increased the broadening of the wave. The slight discrepancy at $t/t_0 = 2.5$ can be explained by the strong interaction between the wave and intrusion at early times.

These simulations of vertically symmetric intrusions are in good agreement with the experimental results presented in Chapter 3 and the heuristic theory for axisymmetric solitary waves presented in Chapter 2. The results are next extended to oceanographic scales in an attempt to capture the essential dy-
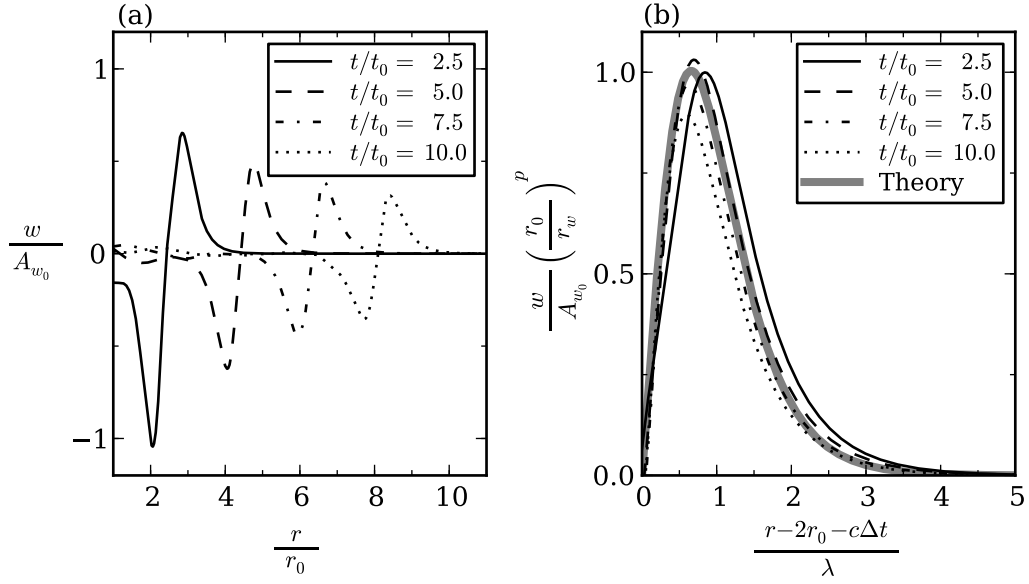
Figure 5.5: (a) Horizontal profiles of the vertical velocity field at a height $z/H = 0.15$ for $\delta_h = 0.2$. (b) Corresponding normalized and shifted profiles, where Δt is the time elapsed since $r_w = 2r_0$, $p = -\frac{1}{2}$ and A_{w_0} is a reference amplitude defined in Fig. 5.4.

namics governing the wave generation process at the mouth of the Columbia River.

Chapter 6

River Plumes

The motivation for this work is based in part on the observations of internal solitary waves by satellite images (Jackson, 2004). Synthetic aperture radar (SAR) images, which detect surface roughness, illustrate that internal solitary waves in many locations of the world's oceans have curved wavefronts. This lateral spreading of the wavefronts occurs when they are generated by a localized source and the motion is not restricted by a rectilinear domain.

As shown by experiments in Chapter 3 and by simulations in Chapter 5, internal solitary waves can be launched by the flow of vertically symmetric intrusions into a two-layer fluid with finite interface thickness. This is a symmetric expansion of a gravity current flowing along the surface of a fluid that consists of a thin stratified layer overlying a deep layer of uniform-density fluid. In nature, such gravity currents can manifest themselves in the form of river plumes flowing into the coastal ocean. For example, in July 2004, measurements of density and velocity fields were taken near the mouth of the Columbia River revealing both the advance of the intruding river into the ocean and the generation of waves at the pycnocline (Nash and Moum, 2005). Details of the specific observations are described in Section 6.1.

Using the numerical code described in Chapter 4, simulations were performed in an attempt to capture the essential dynamics of the Columbia River

plume. To do so, it was necessary to make many crude simplifications to the oceanographic conditions. Regardless of this fact, the dynamics of the motion were captured qualitatively and, for some measurements, quantitatively. Comparisons between the observations and the simulation results are presented in Section 6.4.

6.1 Columbia River Plume

The Columbia River is the fourth largest river in the United States, flowing into the Pacific Ocean at the border of Washington and Oregon. The depth near the river mouth is approximately 20 m, increasing to 100 m within 15 km of the coastline (Pan et al., 2007). The average flow rate from the Columbia River is 7300 m^3/s. However, during the spring months the flow rate may be upwards of 15, 000 m^3/s with ebb currents reaching 3.5 m/s (Jay et al., 2010). SAR images and *in situ* measurements indicate that internal waves, manifest as sinusoidal undulations of the pycnocline, are frequently launched ahead of the plume (Nash and Moum, 2005; Pan et al., 2007; Stashchuk and Vlasenko, 2009), though details of the generation mechanism remain unclear.

Here we focus on the *in situ* measurements that were made on July 23rd, 2004, which are presented in Nash and Moum (2005). Figure 6.1 shows three snapshots of the sea surface temperature, where the plume front is approximated by the black contour. In total, nine transects across the plume front were made, as indicated by the diamonds. Initially, at 17:21UTC, the plume of warm summertime water flowed towards the northwest. At later times (20:22UTC and 21:52UTC) the plume propagated eastward. These directions are indicated in Figure 6.1 by the white velocity vectors.

At each transect of the plume front, a Chameleon turbulence profiler was used to measure the density profiles and an Acoustic Doppler Current Profiler was used to get the velocity profiles. Figure 6.2 shows these measurements at
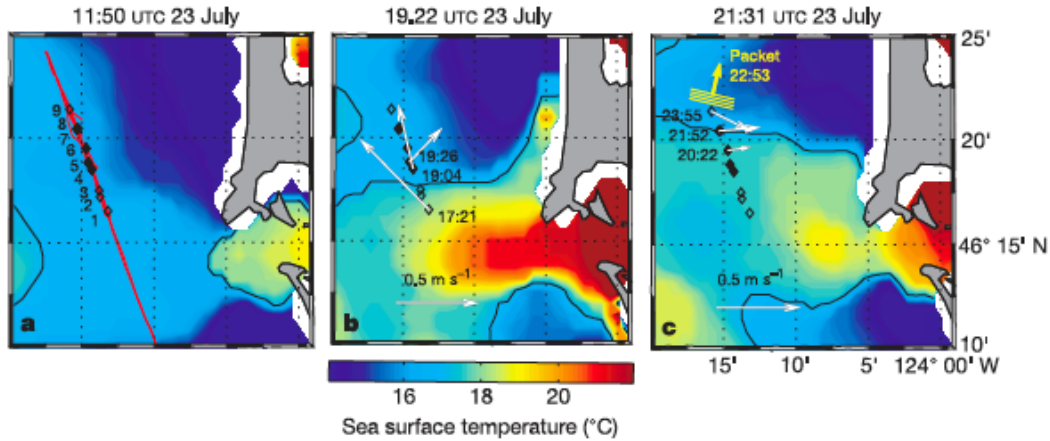
Figure 6.1: Images of the sea surface temperature at the mouth of the Columbia River showing the progression of the plume on July 23rd, 2004 at (a) 11:50, (b) 19:22, and (c) 21:31. The diamonds represent positions where the plume front was crossed and the red line represents the ship track. Measured fluid velocities are indicated by the vectors and the 17°C isotherm, which approximates the plume front, is indicated by the black contour. The domain size of each image is approximately 28 km in the N-S direction and 26 km in the E-W direction. Reprinted by permission from Macmillan Publishers Ltd: Nature Publishing Group, from Figure 2 of Nash, J. D. and J. N. Moum. *Nature.* 437, 400 − 403 (2005).

four crossings. At 19:01UTC (Figure 6.2(a)) the plume flowed at a speed of $U_f \approx 0.6$ m/s against an ambient wind-driven current of $U_a \approx -0.1$ m/s. From the density measurements, it is evident that the plume of fresh water forced the near surface waters to be displaced approximately 20 m downwards. One-and-a-half hours later the plume's speed decreased to 0.4 m/s and the internal wave began to separate from the front (Figure 6.2(b)). The amplitude of the wave at this time was ~ 25 m. Approximately an hour later a second depression of smaller amplitude separated from the plume front and trailed the leading wave by ~ 400 m (Figure 6.2(c)). In the final frame (Figure 6.2(d)) a total of six waves are visible. At the ninth and final transect (not shown), a total of seven waves were measured. All the waves propagated at a nearly constant speed of $c_w \approx 0.45$ m/s. Nash and Moum (2005) also observed that the waves

were rank-ordered in that the largest amplitude wave was at the front of the wave packet and each successive wave had a smaller amplitude. The distance separating contiguous pairs of waves was also rank-ordered.

Using their measurements of the plume's front speed, Nash and Moum (2005) calculated two Froude numbers. The first, $F = U_f/c_w$, was the ratio of the front speed to the measured wave speed. The second, $F_a = U_f/c_a$, was the ratio of the front speed to the theoretical speed of a mode-1 linear wave in the ambient, $c_a \approx 0.4$ m/s. The value of c_a was determined by solving the Taylor-Goldstein equation for the measured background density and velocity fields. The definition of F_a is equivalent to the Froude number, Fr, introduced in Section 2.2, though F_a is based on a measured, not theoretical, intrusion speed. Hence, when $F_a > 1$ the current was supercritical and the generation of solitary waves was expected. Initially, both F and F_a were greater than unity, but as the plume decelerated, the Froude numbers decreased. When $F \approx 1$, at which time $F_a \approx 1.1$, the leading wave separated from the plume front. Nash and Moum (2005) diagnosed wave fission to occur when $F = 1$. Because the definition of F is based on the measured, not the theoretical, wave speed it is not useful in predicting the exact fission location for an arbitrary ambient. However, it is useful to note that F_a is only slightly greater than unity at the time of fission.

The measurements made by Nash and Moum (2005) are summarized in Table 6.1.

6.2   Approximations and the Simulation Setup

The intent here is not to perform a realistic simulation of the Columbia River plume. Rather, it is to use a simple model that attempts to capture the essential dynamics of the wave generation process. Thus many approximations are made. The wind-driven surface currents and topography in the coastal region
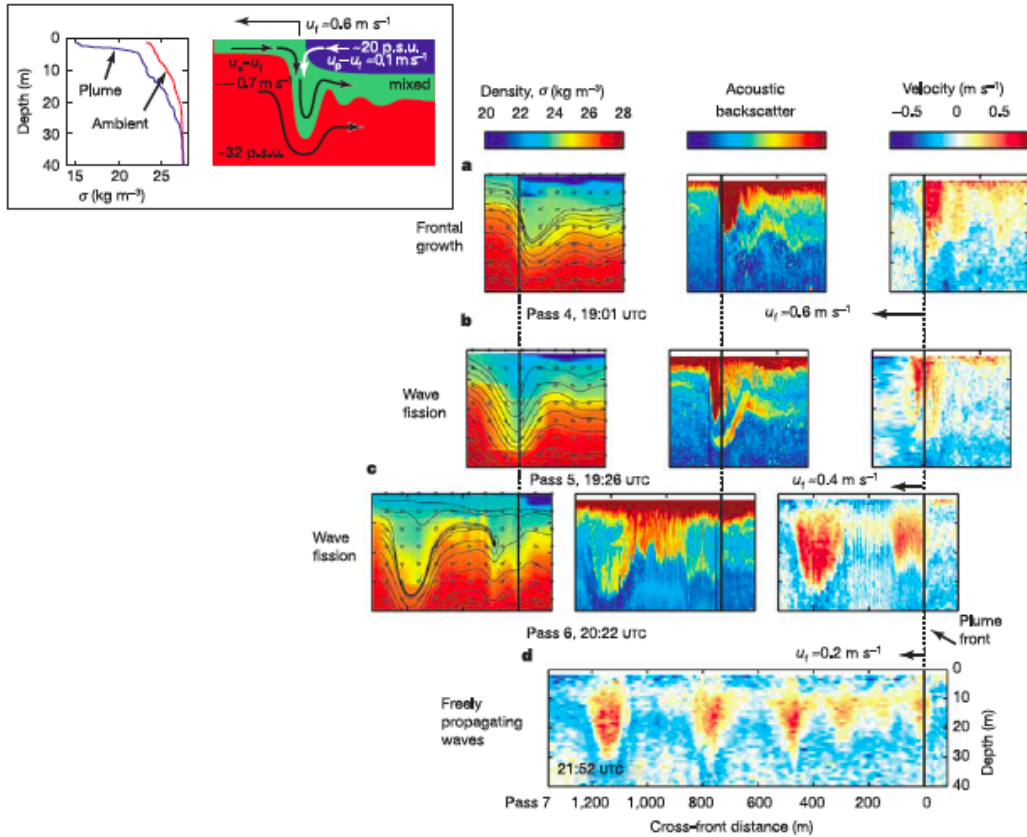
Figure 6.2: Measurements of density, acoustic backscatter and velocity made about 10 km from the mouth of the Columbia River on July 23rd, 2004. (a) Internal waves grow at the front of the plume. (b) Initial separation of the internal wave from the plume front. (c) Separation of a second wave from the plume front. (d) Large amplitude internal waves propagate freely ahead of the plume. The inset shows the density profile that was measured for Pass 4 (panel a). Reprinted by permission from Macmillan Publishers Ltd: Nature Publishing Group, from Figure 3 of Nash, J. D. and J. N. Moum. *Nature*. 437, 400 – 403 (2005).

are omitted: there is no initial ambient motion and the depth is constant. Furthermore, the numerical code requires the background density profile to be constant in r and t, whereas in reality the stratification changes both with location and time.

The forcing conditions also differ significantly. As explained by Nash and Moum (2005), the river plume is released when ebb currents begin to flow, immediately following high tide. Rather than simulate the exact influence of the tides by including a time-variable momentum flux at the source, a partial-depth lock-release initial condition was used to generate the surface gravity current.

Due to the code's boundary conditions that require the flow to be irrotational at the bottom and top of the domain, it is difficult to maintain numerical stability in the simulation of a surface gravity current; the flow is not necessarily irrotational at the front itself. Instead, a vertically symmetric intrusion was simulated and the analysis was carried out in the lower half of the domain where $-\frac{H}{2} \leq z \leq 0$. This symmetry was exploited, for example, in Section 2.1 in the derivation of the rectilinear intrusion speed.

The study of the Columbia River plume by Pan et al. (2007) indicated that the coastal ocean depth in the region where the waves were observed was about 100 m. Therefore the domain half-height was chosen to be $\frac{H}{2} = 100$ m.

Two different background density profiles, which are shown in Figure 6.3 for $z < 0$, were used in these river plume simulations. To ensure that the intruding fluid propagated along $z = 0$, both of the density profiles were odd functions with respect to z about the density at $z = 0$ (not shown).

The initial profile, denoted by $\bar{\rho}_{\mathrm{ST}}(z)$, is an analytic idealization of the actual Columbia River data. The values of the densities were estimated based on the profile presented in the inset of Figure 6.2, where the densities at $z = -5$ m and $z = -40$ m were approximately 1023 kg/m^3 and 1028 kg/m^3,

49
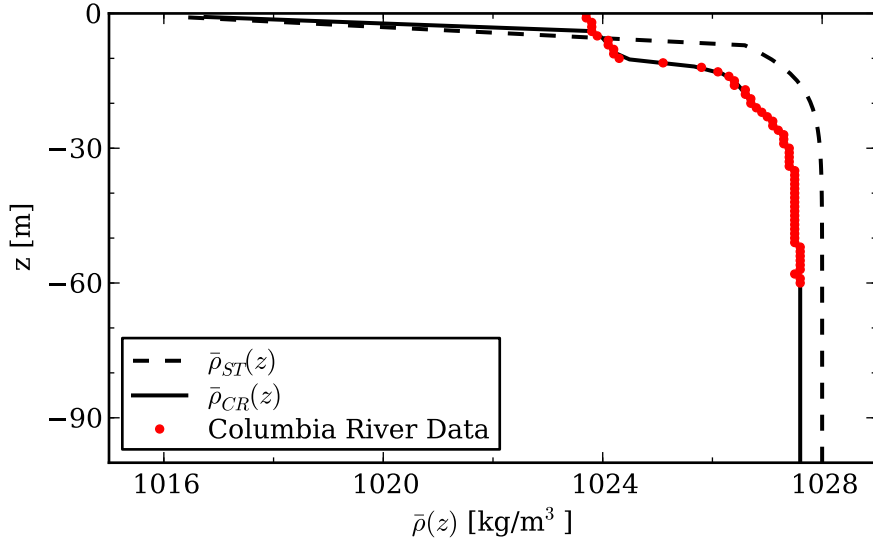
Figure 6.3: The background density profiles, $\bar{\rho}_{\mathrm{ST}}(z)$ and $\bar{\rho}_{\mathrm{CR}}(z)$, used for the river plume simulations in comparison with data measured on July 23, 2004 (Nash and Moum, 2005)(or other reference). Here, only the lower half of the domain, $z < 0$, is shown. The actual profiles were odd functions with respect to z.

respectively. A hyperbolic tangent profile was used for the majority of the simulation profile. However, the density at the three points below $z = 0$ varied linearly in z such that $\bar{\rho}_{\mathrm{ST}}(0) = \rho_i$. This was done to maintain numerical stability by minimizing the magnitude of the density jump at the interface. As is shown in Figure 6.3, $\bar{\rho}_{\mathrm{ST}}(z)$ moderately overestimated the measured densities, but it still captured a thin stratified region overlying a deeper region of constant density.

In the actual data presented in Nash and Moum (2005) the density in the upper 10 m of the ocean was nearly uniform. To examine its influence, additional simulations with a density profile denoted by $\bar{\rho}_{\mathrm{CR}}(z)$ were performed in which the measured data were interpolated onto the computational grid, as shown in Figure 6.3. Below a depth of 60 m, it was assumed that the density was constant because there was no data in this region. Furthermore, the

densities at the two points near the surface were modified to minimize the magnitude of the density jump at $z = 0$.

The initial density field for the simulations was given by

$$\rho_{\text{init}}(r, z) = \begin{cases} \rho_i & 0 < r < r_0, \quad -\frac{H_{\text{m}}}{2} < z < \frac{H_{\text{m}}}{2} \\ \bar{\rho}(z) & \text{elsewhere,} \end{cases} \qquad (6.1)$$

where r_0 is the lock radius and H_{m} is the total height of the mixed region in the lock. In an effort to simulate the scale of the Columbia River plume, the lock diameter, $2r_0$, was chosen to be 5 km, which is the approximate width of the river's mouth. To control the volume of the collapsing fluid, the value of $\frac{H_{\text{m}}}{2}$ was varied from 20 m to 70 m in increments of 10 m. The density of the intruding fluid, ρ_i, was set to 1015 kg/m^3, which was the approximate density of the Columbia River plume on July 23rd, 2004 (Nash and Moum, 2005).

As was described in Section 4.3, a spatially varying viscosity was used to damp out the small scale noise arising from the collapse of the mixed fluid. In order to obtain a nearly uniform Reynolds number, a different viscosity was chosen for each H_{m}. The value of ν_{out} where $r > 3.2$ km increased from 0.02 m^2/s for $\frac{H_{\text{m}}}{2} = 20$ m to 0.09 m^2/s for $\frac{H_{\text{m}}}{2} = 70$ m. For all simulations, the viscosity where $r < 2.7$ km was set to $\nu_{\text{in}} = 5\nu_{\text{out}}$ and between $r = 2.7$ km and $r = 3.2$ km the viscosity varied linearly as given by (4.14). Upon completing the simulations, the Reynolds numbers, $Re = \frac{U_f H_{\text{m}}}{\nu_{\text{out}}}$, were determined to vary between 2070 and 2760. The diffusivity, κ, was chosen so that the Schmidt number, $Sc = \nu_{\text{out}}/\kappa$, was equal to 10 for all simulations. Both the viscosity and the diffusivity were much greater than the physical values in order to maintain numerical stability. The passive tracer diffusivity, κ_{PT}, was set equal to κ for all simulations.

The radial extent of the domain was chosen to be $R = 10$ km because beyond this distance the wave amplitude was sufficiently small that the motion was dominated by viscosity. The grid contained 5000 points in the radial

direction and 128 points in the vertical direction.

The majority of runs simulated the evolution of the river plume and waves for at least 4000 s with a timestep of 0.5 s; however, a timestep of 0.25 s was required to maintain numerical stability for $\frac{H_{\mathrm{m}}}{2} = 70$ m. Snapshots of the density, velocity and vorticity fields were output every 10 s. Due to the large domain size, each simulation took at least 8 days to complete.

6.3 Analysis and Results

Qualitatively similar to observations, the propagation of the simulated river plume launched a train of freely propagating internal waves. This is shown for $\frac{H_{\mathrm{m}}}{2} = 50$ m in Figure 6.4 for a simulation with analytically prescribed ambient density ($\bar{\rho} = \bar{\rho}_{\mathrm{ST}}$) and in Figure 6.5 for a simulation with interpolated Columbia River ambient density ($\bar{\rho} = \bar{\rho}_{\mathrm{CR}}$). In these figures, the black line denotes the 1023 kg/m^3 isopycnal.

More waves were launched in the simulation using $\bar{\rho} = \bar{\rho}_{\mathrm{ST}}$ than in the simulation using $\bar{\rho} = \bar{\rho}_{\mathrm{CR}}$. This comparison is consistent for all values of $\frac{H_{\mathrm{m}}}{2}$, as shown in Table 6.1. The reason less waves appear when $\bar{\rho} = \bar{\rho}_{\mathrm{CR}}$ can be attributed to the structure of the upper mixed region in that ambient density profile. The large density jump at $z \approx -10$ m can be approximated by a strongly stratified region between two layers of uniform density. When long waves propagate in such an ambient fluid, shear is introduced across the stratified interface. This shear causes the flow to go unstable which, in turn, causes some of the wave energy to be converted into mixing. The necessary condition for the instability of a parallel stratified shear flow is that the Richardson number satisfies Ri $\lesssim 1/4$. Generalizing the definition of Ri, at all points in the domain we estimate

$$\mathrm{Ri}(r, z) \approx \frac{N_{\mathrm{T}}^2}{\zeta^2}, \tag{6.2}$$
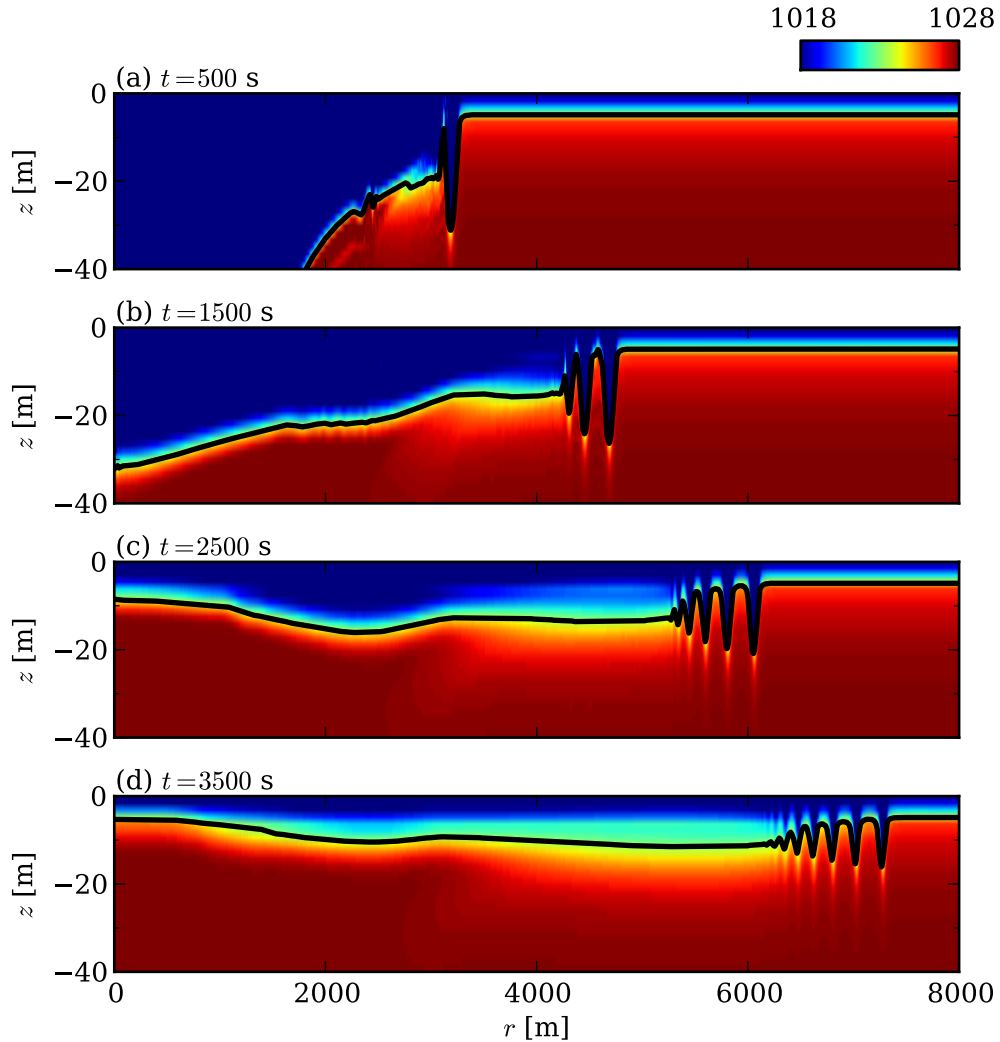
Figure 6.4: Snapshots of the total density field in units of kg/m^3 from a simulation with $\bar{\rho} = \bar{\rho}_{\text{ST}}$ and $\frac{H_{\text{m}}}{2} = 50$ m. The black line is the 1023 kg/m^3 isopycnal. Only a subsection of the total domain is shown as $R = 10\,000$ m and $\frac{H}{2} = 100$ m. It should be noted that the simulated plume is propagating from left to right in this figure, whereas the observed plume in Figure 6.2 is propagating from right to left.
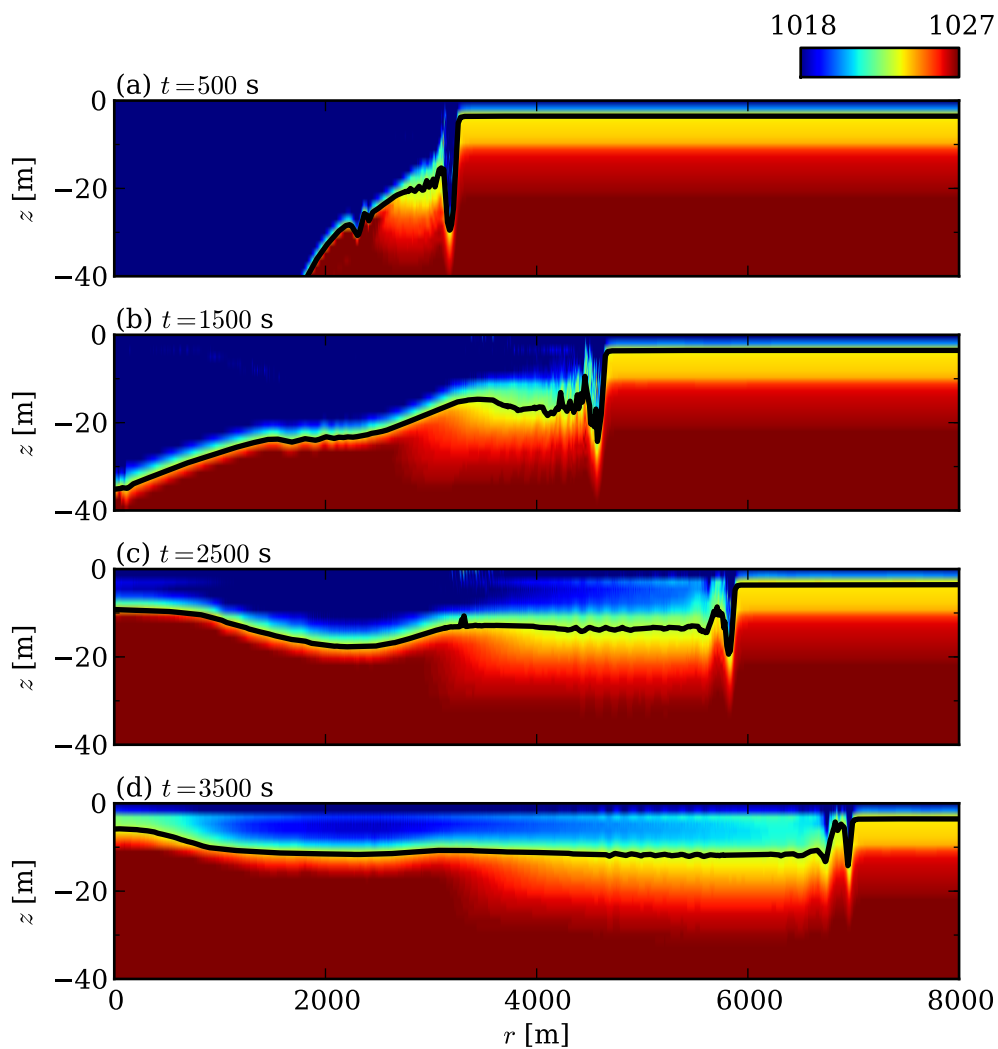
Figure 6.5: As in Figure 6.4, but showing snapshots from a simulation with $\bar{\rho} = \bar{\rho}_{\mathrm{CR}}$. The upper limit of the colour map is also reduced to $1027\,\mathrm{kg/m^3}$.
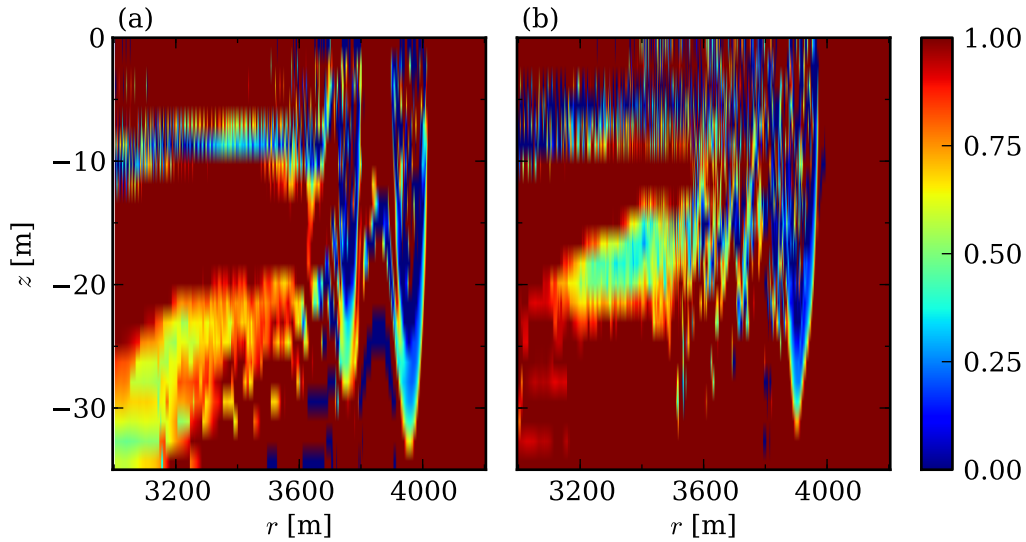
Figure 6.6: The local Richardson number, given by (6.2), near the front of the river plume at $t = 1000$ s for $\frac{H_{\mathrm{m}}}{2} = 50$ m with (a) $\bar{\rho} = \bar{\rho}_{\mathrm{ST}}$ and (b) $\bar{\rho} = \bar{\rho}_{\mathrm{CR}}$. The unstable regions where $Ri \lesssim 0.25$ suggest that there is strong mixing near the plume's head, especially in (b).

where N_{T} is the local buoyancy frequency based on the background and perturbation density gradients and ζ is the local vorticity. The value of Ri at $t = 1000$ s for $\frac{Hm}{2} = 50$ m is plotted in Figure 6.6(a) for $\bar{\rho} = \bar{\rho}_{\mathrm{ST}}$ and Figure 6.6(b) for $\bar{\rho} = \bar{\rho}_{\mathrm{CR}}$. The low Richardson numbers in these figures are highly suggestive of mixing. However, the small scale shear-unstable disturbances were not explicitly resolved due to the necessarily high viscosity of the simulations. By comparing Figures 6.6(a) and (b), it can be argued that the flow is more unstable when $\bar{\rho} = \bar{\rho}_{\mathrm{CR}}$. This is also apparent in the profile of the isopycnals shown in Figure 6.5. Due to the increased flux of energy to small scales by mixing, which is further enhanced by viscosity, less energy was available for wave formation in the simulations with $\bar{\rho} = \bar{\rho}_{\mathrm{CR}}$ and hence, fewer waves were formed.

The initial speed, U_f, of the river plume for all the simulations were determined by locating the position of its front, r_f, at each time and then calculating
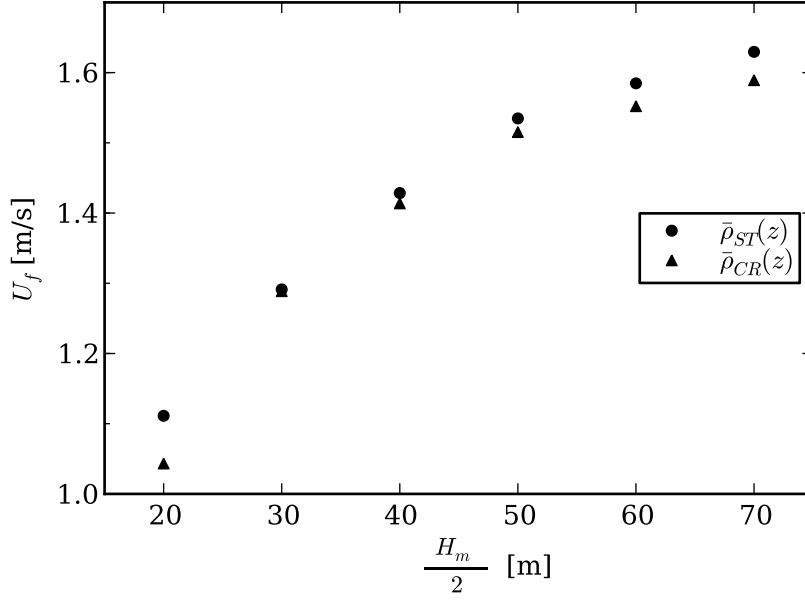
Figure 6.7: Initial speeds of the leading wave, and hence the river plume, as determined by calculating $\mathrm{d}r_f/\mathrm{d}t$ from $t = 150$ s to $t = 450$ s.

the slope, $\mathrm{d}r_f/\mathrm{d}t$, between $t = 150$ s and $t = 450$ s. These speeds are plotted versus $\frac{H_m}{2}$ in Figure 6.7. This shows that U_f increases with $\frac{H_m}{2}$, as expected, because the initial available potential energy that is partially converted to kinetic energy of the plume is proportional to H_m^2. Figure 6.7 also shows that, for given $\frac{H_m}{2}$, the river plume in the ambient with $\bar{\rho} = \bar{\rho}_{\mathrm{ST}}$ travelled on average 2% faster than those in ambients with $\bar{\rho} = \bar{\rho}_{\mathrm{CR}}$. The relatively small difference in speeds implies that the advance of the plume is relatively insensitive to the structure of the density profiles that were used.

The analysis of these simulations involved calculating the speed and amplitude of each wave for various times. To do so, the location of the 1023 kg/m^3 isopycnal was found every 10 s. From the resulting profile, the position of each wave was determined from the radial location of each local minima. The wave position r_w was then plotted versus time, as shown in Figure 6.8(a) for $\frac{H_m}{2} = 50$ m and $\bar{\rho} = \bar{\rho}_{\mathrm{ST}}$.

56

For each wave, the average speed c_w was calculated every 300 s by calculating the slope, $\mathrm{d}r_w/\mathrm{d}t$, over a 300 s interval. As shown in Figure 6.8(b), the wave speeds decreased with time and eventually all the waves attained a similar speed. The initial speeds of the leading waves were equal to the front speed, U_f, because the plume and the wave initially propagated together. Eventually, the wave separated from the plume front. Admittedly, though, it was difficult to determine the exact location of wave fission because the density of the intruding plume was the same as that just ahead of it. Furthermore, the high diffusivity of the passive tracer field made it an unreliable indictor for the location of the plume at late times.

Figure 6.4 shows that waves develop successively, one after the other, eventually forming a wave train of crests and troughs. This is quantified in Figure 6.8. The leading wave is launched almost immediately (at $t \approx 60$ s) whereas the second wave forms around $t \approx 550$ s. At this time, the second wave is approximately 130 m behind the first and, because the leading wave is initially travelling faster than the second wave (see Figure 6.8(b)), the distance separating the waves grows. The maximum separation distance $\Delta r_{12} \approx 250$ m is eventually attained when the waves reach a similar speed. This trend was observed for all the simulations with $\bar{\rho} = \bar{\rho}_{\mathrm{ST}}$ and the Δr_{12} values are given in Table 6.1. For these simulations, the separation distance does not depend significantly on $\frac{H_{\mathrm{m}}}{2}$. All values lie between 210 m and 280 m, suggesting that Δr_{12} is set by the background density profile, not the speeds of the waves. Additional measurements (not shown) indicate that the distance separating successive waves decreases (ie. $\Delta r_{12} > \Delta r_{23} > \Delta r_{34}$).

The approximate values of Δr_{12} are given in Table 6.1 for the simulations with $\bar{\rho} = \bar{\rho}_{\mathrm{CR}}$. Due to the enhanced mixing that occurs in these simulations, it was sometimes difficult to locate the exact position of the waves. In some cases a steady separation distance was not attained in the time of the simulation.
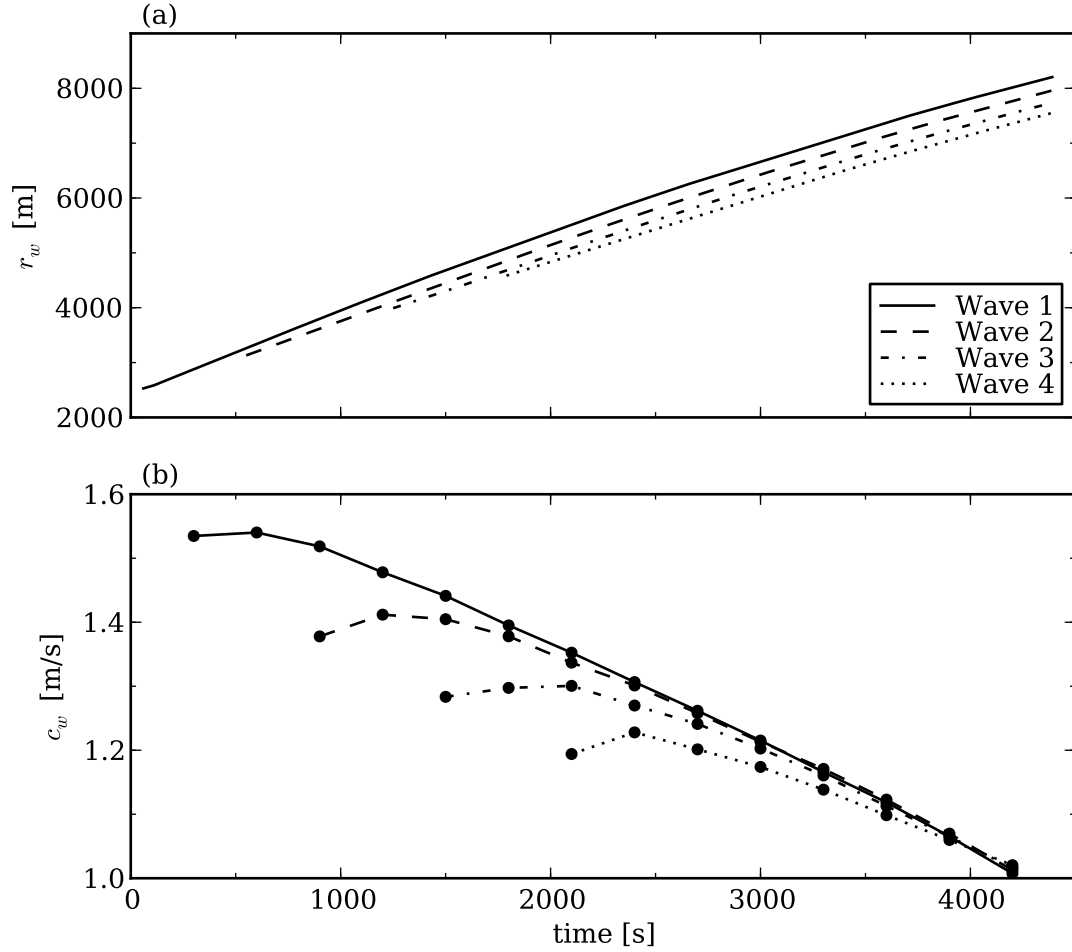
Figure 6.8: Six waves were formed in the simulation with $\frac{H_m}{2} = 50$ m and $\bar{\rho} = \bar{\rho}_{\mathrm{ST}}$ (see Figure 6.4). The positions, r_w, of the first four waves were measured from $r = 0$ are plotted versus time in (a) and the average speeds, c_w, of the first four waves which were calculated every 750 s are shown in (b). In comparison, the mode-1 wave speed, c_a, for $\bar{\rho} = \bar{\rho}_{\mathrm{ST}}$ is 0.67 m/s.
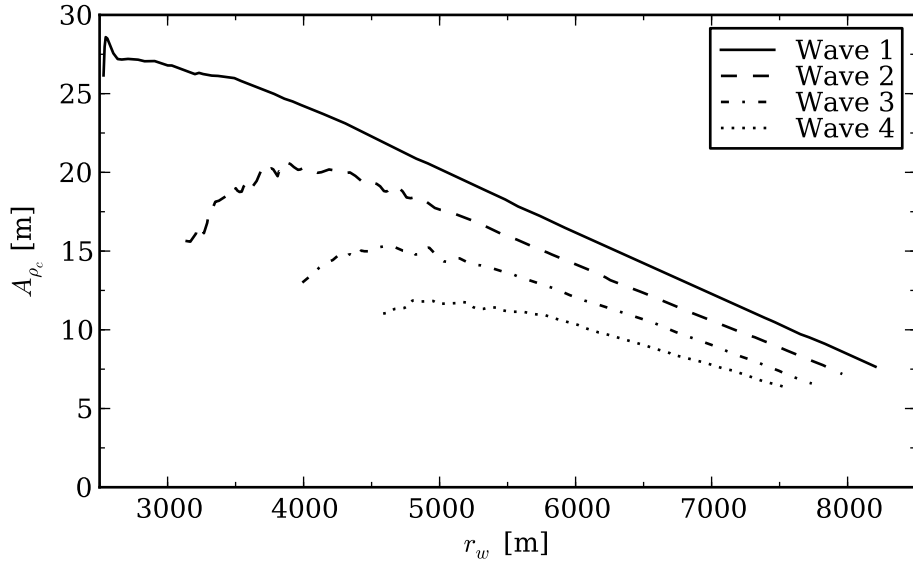
Figure 6.9: The magnitude of the isopycnal displacement for $\rho_c = 1023$ kg/m^3 versus position for the simulation with $\bar{\rho} = \bar{\rho}_{\mathrm{ST}}$ and $\frac{H_{\mathrm{m}}}{2} = 50$ m. Although six waves were observed (see Figure 6.4), only the amplitude for the first four waves is plotted.

This is indicated in Table 6.1 by the asterisks.

In the snapshots in Figures 6.4 and 6.5 it is evident that the amplitudes of the waves decrease as they propagate outwards. The displacement of the isopycnal troughs were measured relative to the upstream position, and are plotted versus position in Figure 6.9 for the simulation shown in Figure 6.4. After an initial increase in amplitude during the generation of the wave, the amplitude decreases approximately linearly with r. It is expected that the amplitude should obey an inverse power law for sufficiently large r. In particular, a single inviscid wave should decay in amplitude as $r^{-1/2}$. However, the simulations were not run long enough to observe this trend. Due to the damping of the motion by the artificially high viscosity we expect the amplitude to decay more rapidly than $A \sim r^{-1/2}$.

It is also evident in both Figures 6.4 and 6.9, that at any given time the waves are rank-ordered. That is, the amplitude of each successive wave is

59

smaller than the one ahead it (ie. $A_1 > A_2 > A_3$). The maximum amplitudes of the leading waves, $A_{max} = \max(A_1)$, for all the simulations are summarized in Table 6.1. As expected, the maximum wave amplitude increases with increasing $\frac{H_{\mathrm{m}}}{2}$. Furthermore, A_{max} does not vary significantly between simulations with the two different background density profiles.

6.4   Discussion

Despite the omission of tides, surface currents and bottom topography, the simulations were in good qualitative, and in somewhat good quantitative agreement with the observations presented in Nash and Moum (2005). In this section, the observations discussed in Section 6.1 will be compared to the simulations with $\frac{H_{\mathrm{m}}}{2} = 50$ m because the initial amplitudes of the observed and simulated wave were approximately equal (see Table 6.1).

Figures 6.4 and 6.5 clearly show that the surface-propagating gravity current launches a train of freely-propagating internal waves which are formed in succession, qualitatively consistent with the observations of Nash and Moum (2005).

Nash and Moum (2005) observed a total of seven freely propagating waves. In comparison, the number of waves in the simulations varied from 2 to 6 with less (2–3) waves being generated in simulations with $\bar{\rho} = \bar{\rho}_{\mathrm{CR}}$, the ambient density interpolated from the observed data. There are several possible reasons for this discrepancy. As explained in Section 6.3, there appeared to be enhanced mixing in simulations with $\bar{\rho} = \bar{\rho}_{\mathrm{CR}}$, which reduced the amount of energy available for wave formation. Furthermore, the measured density profile shown in Figure 6.3 was observed at a specific instant in time at a specific location, whereas the stratification likely varied throughout the observation region, having a significant effect on wave formation. The wind-driven surface currents that were observed by Nash and Moum (2005) also helped the wave

$\frac{H_{\mathbf{m}}}{2}$ (m)	**Speed** U_f (m/s)	**Amplitude** A_{max} (m)	**Wave Separation** Δr_{12} (m)	**No. of Waves**
		Columbia River Observations		
	0.7	20 - 25	400	7
		$\bar{\rho}_{\mathrm{ST}}(z)$		
20	1.1	11	220	6
30	1.3	17	210	6
40	1.4	22	240	6
50	1.5	27	250	6
60	1.6	32	260	5
70	1.6	36	280	5
		$\bar{\rho}_{\mathrm{CR}}(z)$		
20	1.0	11	150	3
30	1.3	16	150*	3
40	1.4	23	170	3
50	1.5	29	220	2
60	1.6	34	280	2
70	1.6	38	250*	3

Table 6.1: Data from the river plume simulations in comparison with the observations made by Nash and Moum (2005). The initial speed of the river plume is denoted by U_f. For the observations, U_f was measured at 17:21UTC and for the simulations U_f was computed at $t = 300$ s. The maximum displacement of the 1023 kg/m^3 isopycnal of the leading wave is denoted by A_{max} and the maximum separation distance attained between the first and second waves is denoted by Δr_{12}. The * indicates that the separation distance was increasing or decreasing rather than remaining constant.

formation by increasing the convergence of horizontal velocities at the plume front. Of all these reasons, it is most likely the artificially high viscosities that caused fewer waves to form in the simulations. At late times, when the wave amplitudes and speeds were small, the motion was significantly damped preventing the formation of additional waves. This conclusion was made on the basis of simulations (not shown) with still higher viscosities, in which only 1–2 waves formed.

The simulated location of the initial wave fission is significantly different from the observed location with respect to the river mouth. As shown in Figure 6.2(b), the leading wave separated from the plume front at roughly 19:25UTC, at which time the plume was roughly $12 - 15$ km from the mouth of the Columbia River (determined from Figure 6.1). In simulations, the initial wave fission occurred within 500 m of the lock (for $\frac{H_m}{2} = 50$ m). As mentioned in Section 6.3, it was difficult to determine the exact location of wave fission from the simulations because the density of the intruding fluid was the same as that just ahead of it. Because the second wave formed around $r = 3000$ m (see Figure 6.8), it was assumed that the wave fission occurred prior to the intrusion reaching this location. The reason for the discrepancy between the simulations and the observations is likely due to the initial conditions: the simulations used an instantaneous constant-volume release to generate a gravity current, whereas the Columbia River plume is better represented by gradual increase in volume flux at the source while the tide ebbs. Based on a mean flow rate of 1 m/s and a semidiurnal tide (Jay et al., 2010), the maximum volume flux occurs approximately 3.1 hours following high tide at a distance of 11 km from the mouth of the Columbia River. It is at this location that a lock-release best describes the plume. Therefore, it can be argued that the simulation results are consistent with the observation of waves being generated $12 - 15$ km from the mouth of the river.

Another comparison can be made in regards to the plume speeds and Froude numbers. Although the initial front speed measurements differ by up to a factor of 2 (see Table 6.1), the river plume decelerates as it propagates outwards in both the simulations and the observations. On the other hand, the observed wave speeds were approximately constant at 0.45 m/s, while the simulated initial wave speed for $\frac{H_{\mathrm{m}}}{2} = 50$ m was 1.5 m/s and then decreased throughout the simulation by up to 50%, as shown in Figure 6.8(b). The decreasing values of c_w in time make it difficult to determine a Froude number with respect to the wave speed, $F = U_f/c_w$, as was done by Nash and Moum (2005).

It is possible, however, to calculate a linear long wave speed for the ambient, c_a, by solving the Taylor-Goldstein equation. To do so, a Matlab program (Smyth et al., 2010) was used to calculate the mode-1 wave speed. Explicitly, $c_a \simeq 0.67$ and 0.65 m/s for $\bar{\rho} = \bar{\rho}_{\mathrm{ST}}$ and $\bar{\rho}_{\mathrm{CR}}$, respectively. In comparison, Nash and Moum (2005) calculated $c_a \simeq 0.4$ m/s, but this computation included the measured background horizontal velocity field. For all the simulations, the initial plume speeds were significantly larger than c_a (see Figure 6.7). Hence, $F_a > 1$ and solitary waves were launched. Due to the high diffusivity of the passive tracer field, it was difficult to measure the plume speeds, and consequently F_a, at late times. However, the speeds of the waves (shown in Figure 6.8) suggest that $F_a > 1.5$ for the entire duration of the simulation. In comparison, Nash and Moum (2005) observed that the initial wave separated from the front of the plume when $F_a \approx 1.1$ and F_a decreased to less than unity by the fifth measurement of the plume's speed.

Nash and Moum (2005) measured a $20 - 25$ m amplitude for the leading wave, which compared well with the simulations in cases where $\frac{H_{\mathrm{m}}}{2}$ was equal to 40 m or 50 m. In the simulations, the wave amplitude decreased rapidly as shown in Figure 6.9. However, Nash and Moum (2005) reported that the

amplitude remained constant for nearly 5 km. Due to the axisymmetric geometry, the amplitude decay is expected. Therefore, their observed constant amplitude must be attributed to other factors. A possible explanation is that at the time of the measurements, the observed wave front (black line in Figure 6.1) is more or less planar; since the wave is not spreading radially, a constant amplitude would be expected.

There is qualitatively good agreement between the observations and the simulations in that the amplitude of each successive wave was smaller than the one ahead of it. This is apparent in Figure 6.2(d) for the observed waves and in Figure 6.9 for the simulated waves. The decreased amplitude can be attributed to the reduced convergence at the front of each wave and the observation of rank-ordered waves is consistent with other observations of solitary wave packets (Jackson, 2004).

A final comparison between the observations and the simulations can be made with respect to the spacing between contiguous waves. Figure 6.2(d) shows that the maximum distance between the leading wave and the second wave, Δr_{12}, is about 400 m. In comparison, the maximum distance measured in the simulations varies between 150 m and 280 m. Although the magnitude of the separation is significantly different, both the simulations and the observations show that the distance between successive waves decreases.

In general, despite the approximations of the numerical model, the simulations were found to be in good qualitative agreement with the observations: the propagation of a river plume into the coastal ocean launches a train of freely-propagating internal waves that are rank-ordered with respect to their amplitudes and separation distances. Because the intent of these simulations was to capture the essential dynamics of the wave generation process, we can also argue, for $\frac{H_m}{2} = 40$ m or 50 m, that the wave characteristics are is good quantitative agreement with the observed wave speeds and amplitudes.

Chapter 7

Summary and Conclusions

We have studied the dynamics of axisymmetric internal solitary waves by way of theory, experiments and numerical simulations. Although this work was motivated by the observation of curved wave fronts advancing ahead of river plumes in the coastal ocean, we began by investigating the launch of these waves by vertically symmetric intrusions in a two-layer fluid with finite interface thickness. We then adapted the idealized study to more realistic oceanographic circumstances and compared the results with observations of the Columbia River plume.

In the study of vertically symmetric intrusions, a theory was derived to predict the speed of such an intrusion as a function of the interface thickness. Unlike previous estimates (Ungarish, 2005; White and Helfrich, 2008), our theoretical prediction was in agreement with the recent experiments by Bolster et al. (2008).

Laboratory experiments and numerical simulations of vertically symmetric intrusions were conducted in a cylindrical geometry. In agreement with the theory, the intrusion speed was dependent upon the non-dimensional thickness of the interface, decreasing from $0.8U_0$ to $0.5U_0$ as δ_h increased from 0 to 1. These speeds were up to 20% slower than those of intrusions in a rectilinear geometry.

From the observation that the experimental intrusions propagated well beyond 3 lock radii at a constant speed, it was hypothesized that a closed-core solitary wave surrounded the intrusion and carried it outwards. In addition to confirming the presence of this wave at interfaces satisfying $0 < \delta_h \lesssim 0.4$, the simulations were used to obtain more information about the wave characteristics. The wave carried the intrusion to approximately 7 lock radii as its amplitude decreased as $r^{-1/2}$, a power law consistent with energy conservation. Beyond this distance, the intrusion ran out of fluid and decelerated to a stop, whereas the wave continued to propagate at a constant speed. Due to the additional effect of linear dispersion, the rate of wave amplitude decay increased to r^{-1} beyond 7 lock radii.

Profiles of the wave just above the intrusion head were compared to a rectilinear solitary wave KdV theory adapted to a cylindrical geometry in which the wave amplitude decreased as $r^{-1/2}$. The wave profiles collapsed onto a theoretical curve suggesting that the amplitude decay was slow enough that it did not significantly affect the propagation of the wave. From a single measurement of wave amplitude and the assumption that the amplitude decays as $r^{-1/2}$, this heuristic KdV theory is able to predict the amplitude, speed and spread of the wave during its nonlinear evolution phase after generation. The fact that the solitary wave evolved in a manner closer to the heuristic prediction than to the rigorous cylindrical solitary wave equation suggests that a different mathematical approach should be taken in developing an appropriate weakly nonlinear theory. Because the adapted KdV theory did not account for the leaky closed-core behaviour of the wave, it is suggested that future investigation could adapt the Dubreil-Jacotin-Long equation to a cylindrical geometry; this equation has been used to describe closed-core (Davis and Acrivos, 1967; Tung et al., 1982) and leaky (Derzho and Grimshaw, 2007) solitary waves in a rectilinear geometry.

The numerical code was also used to simulate a river plume emanating from the mouth of the Columbia River. In essence, this involved prescribing more realistic ambient density profiles and allowing the intrusion to emanate from a partial-depth mixed region. In contrast to the simulations of vertically symmetric intrusions, which launched a single wave, a freely propagating train of internal solitary waves was launched by the simulated river plume.

The development of a freely propagating train of waves was consistent with the observations made by Nash and Moum (2005) in July 2004 of a plume emanating from the Columbia River. There was also qualitative agreement between the simulations and the observations in that the waves formed one at a time with each successive wave having a smaller amplitude. Furthermore, the separation distance between contiguous waves decreased with each successive wave pair. Quantitatively, it can be argued that the magnitudes of the speeds and amplitudes are of the same order. This was somewhat surprising considering the number of approximations that were made. In particular, wind-driven surface currents and bottom topography were omitted in the simulations. Furthermore, a constant-volume lock-release was used to simulate the river outflow and a constant stratification (in r and t) was used for the ambient fluid. These limitations had the most effect in the Froude number criterion for wave fission. Nash and Moum (2005) observed that the leading wave separated from the plume when $F_a \approx 1.1$ and eventually F_a was less than unity. In contrast, $F_a > 1.5$ for the duration of the simulations.

Further investigation is necessary to generalize our results to make predictions about the realistic propagation of river plumes in the coastal ocean. A better understanding of the dynamics of these plumes and the waves they generate is important for predicting the transport of nutrients, sediments and pollutants in the local region. Higher resolution simulations with lower viscosity would be beneficial as the motion of the river plume at late times seemed

to be dominated by viscosity. More specifically, the fact that the amplitude decayed more rapidly than $r^{-1/2}$ suggests that energy was being dissipated due to viscosity. It would also be useful to have *in situ* data for plumes emanating from different rivers. This could provide additional insight into how parameters such as stratification, wind-driven currents, or bottom topography affect the formation and propagation of the waves. At this time, however, only the Columbia River plume has been examined in detail for its ability to generate internal solitary waves.

Bibliography

Benjamin, T. B. (1968). Gravity currents and related phenomena. *J. Fluid Mech. 31*, 209–248.

Benney, D. J. (1966). Long nonlinear waves in fluid flows. *J. Math. and Phys. 45*, 52–63.

Bolster, D., A. Hang, and P. F. Linden (2008). The front speed of intrusions into a continuously stratified medium. *J. Fluid Mech. 594*, 369–377.

Britter, R. E. and J. E. Simpson (1981). A note on the structure of the head of an intrusive gravity current. *J. Fluid Mech. 112*, 459–466.

Davis, R. E. and A. Acrivos (1967). Solitary internal waves in deep water. *J. Fluid Mech. 29*, 593–607.

Derzho, O. G. and R. Grimshaw (2007). Asymmetric internal solitary waves with a trapped core in deep fluids. *Phys. Fluids 19*, Art. No. 095102.

Didden, N. and T. Maxworthy (1982). The viscous spreading of plane and axisymmetric gravity currents. *J. Fluid Mech. 121*, 27–42.

Dubreil-Jacotin, M. K. (1937). Sur les thèoremes d'existence relatifs aux ondes permanentes pérodiques à deux dimensions dans les liquides hétérogènes. *J. Math. Pures Appl. 16*, 43.

Faust, K. M. and E. J. Plate (1984). Experimental investigation of intrusive

gravity currents entering stably stratified fluids. *J. Hydraul. Res. 22*(5), 315–325.

Hallworth, M. A., H. E. Huppert, J. C. Phillips, and R. S. J. Sparks (1996). Entrainment into two-dimensional and axisymmetric turbulent gravity currents. *J. Fluid Mech. 308*, 289–311.

Halpern, D. (1971). Observations of short period internal waves in Massachusetts Bay. *J. Mar. Res. 29*, 116–132.

Helfrich, K. R. and W. Melville (2006). Long nonlinear internal waves. *Annu. Rev. Fluid Mech. 38*, 395–425.

Hoult, D. P. (1972). Oil spreading on the sea. *Ann. Rev. Fluid Mech. 4*, 341–368.

Huppert, H. E. (1982). The propagation of two-dimensional and axisymmetric viscous gravity currents over a rigid horizontal surface. *J. Fluid Mech. 121*, 43–58.

Huppert, H. E. and J. E. Simpson (1980). The slumping of gravity currents. *J. Fluid Mech. 99*, 785–799.

Huq, P. (1996). The role of aspect ratio on entrainment rates of instantaneous, axisymmetric finite volume releases of dense fluid. *J. Hazardous Mater. 49*, 89–101.

Jackson, C. R. (2004). An atlas of internal solitary-like waves and their properties (2nd ed.). Technical report, Global Ocean Associates. Available online at www.internalwaveatlas.com.

Jay, D. A., E. D. Zaron, and J. Pan (2010). Initial expansion of the Columbia River tidal plume: Theory and remote sensing observations. *J. Geophys. Res. 115*, Art. No. C00B15.

Long, R. R. (1953). Some aspects of the flow of stratified fluids. I. A theoretical investigation. *Tellus 5*, 42–58.

Long, R. R. (1956). Solitary waves in one- and two-fluid systems. *Tellus 8*, 460–471.

Lowe, R. J., P. F. Linden, and J. W. Rottman (2002). A laboratory study of the velocity structure in an intrusive gravity current. *J. Fluid Mech. 456*, 33–48.

Maxworthy, T. (1980). On the formation of nonlinear internal waves from the gravitational collapse of mixed regions in two and three dimensions. *J. Fluid Mech. 96*, 47–64.

McMillan, J. M. and B. R. Sutherland (2010). The lifecycle of axisymmetric internal solitary waves. *Nonlin. Proc. Geophys. 17*, 443–453.

Mehta, A., B. R. Sutherland, and P. J. Kyba (2002). Interfacial gravity currents. II. Wave excitation. *Phys. Fluids 14*, 3558–3569.

Miles, J. W. (1978). An axisymmetric Boussinesq wave. *J. Fluid Mech. 84*, 181–191.

Nash, J. D. and J. N. Moum (2005). River plumes as a source of large-amplitude internal waves in the coastal ocean. *Nature 437*, 400–403.

Pan, J., D. A. Jay, and P. M. Orton (2007). Analyses of internal solitary waves generated at the columbia river plume front using SAR imagery. *J. Geophys. Res. 1112*, Art. No. C07014.

Patterson, M. D., J. E. Simpson, S. B. Dalziel, and G. L. F. van Heijst (2006, APR). Vortical motion in the head of an axisymmetric gravity current. *Phys. Fluids 18*(4), Art. No. 046601.

Perry, R. B. and G. R. Schimke (1965). Large amplitude internal waves observed off the north-west coast of Sumatra. *J. Geophys. Res. 70*, 2319–2324.

Rooij, F., P. F. Linden, and S. B. Dalziel (1999). Saline and particle-driven interfacial intrusions. *J. Fluid Mech. 389*, 303–334.

Rottman, J. W. and J. E. Simpson (1983). Gravity currents produced by instantaneous releases of a heavy fluid in a rectangular channel. *J. Fluid Mech. 135*, 95–110.

Simpson, J. E. (1997). *Gravity Currents* (2nd ed.). Cambridge, England: Cambridge University Press.

Smyth, W. D., J. N. Moum, and J. D. Nash (2010). Narrowband oscillations in the upper equatorial ocean. Part II: Properties of shear instabilities. *J. Phys. Oceanogr.*, Submitted June 29.

Stashchuk, N. and V. Vlasenko (2009). Generation of internal waves by a supercritical stratified plume. *J. Geophys. Res. 114*, Art. No. C01004.

Sutherland, B. R. and J. T. Nault (2007). Intrusive gravity currents propagating along thin and thick interfaces. *J. Fluid Mech. 586*, 109–118.

Tung, K. K., T. F. Chan, and T. Kubota (1982). Large amplitude internal waves of permanent form. *Stud. Appl. Math. 66*, 1–44.

Ungarish, M. (2005). Intrusive gravity currents in a stratified ambient: Shallow-water theory and numerical results. *J. Fluid Mech. 535*, 287–323.

Ungarish, M. (2006). On gravity currents in a linearly stratified ambient: A generalization of Benjamin's steady-state propagation results. *J. Fluid Mech. 548*, 49–68.

Weidman, P. D. and M. G. Velarde (1992, Feb). Internal solitary waves. *Stud. Appl. Math. 86* (2), 167–184.

Weidman, P. D. and R. Zakhem (1988). Cylindrical solitary waves. *J. Fluid Mech. 191*, 557–573.

White, B. L. and K. R. Helfrich (2008). Gravity currents and internal waves in a stratified fluid. *J. Fluid. Mech. 616*, 327–356.

Zemach, T. and M. Ungarish (2007). On axisymmetric intrusive gravity currents: The approach to self-similarity solutions of the shallow-water equations in a linearly startified ambient. *Proc. R. Soc. A 463*, 2165–2183.

Zhang, L. Z., L. Zeng, B. Zhang, Z. Li, and Z. L. Luo (2010). Numerical study on head advancement of axisymmetric gravity currents. *Communications in Nonlinear Science and Numerical Simulation 15* (7), 1893–1898.

Ziegenbein, J. (1969). Short internal waves in the Strait of Gibraltar. *Deep Sea Res. 16*, 479 – 487.